nuclear fusion
IAEA

PAPER • OPEN ACCESS

Overview of T and D–T results in JET with ITER-like wall

To cite this article: C.F. Maggi *et al* 2024 *Nucl. Fusion* **64** 112012

View the article online for updates and enhancements.

You may also like

- The role of shear flow collapse and enhanced turbulence spreading in edge cooling approaching the density limit
Ting Long, P.H. Diamond, Rui Ke et al.
- Divertor Tokamak Test facility project: status of design and implementation
Francesco Romanelli, on behalf of DTT Contributors, D. Abate et al.
- Overview of the EUROfusion Tokamak Exploitation programme in support of ITER and DEMO
E. Joffrin, M. Wischmeier, M. Baruzzo et al.

This content was downloaded from IP address 155.253.32.3 on 16/10/2024 at 14:37

OPEN ACCESS
IOP Publishing | International Atomic Energy Agency
Nuclear Fusion
Nucl. Fusion **64** (2024) 112012 (32pp)
https://doi.org/10.1088/1741-4326/ad3e16

Overview of T and D–T results in JET with ITER-like wall

C.F. Maggi[1,*], D. Abate[2], N. Abid[1], P. Abreu[3], O. Adabonyan[1], M. Afzal[1], I. Ahmad[1], M. Akhtar[1], R. Albanese[4], S. Aleiferis[1], E. Alessi[5], P. Aleynikov[6], P. Aleynikov[7], J. Alguacil[8], J. Alhage[9], M. Ali[1], H. Allen[1], M. Allinson[1], M. Alonzo[10], E. Alves[3], R. Ambrosino[4], E. Andersson Sundén[11], P. Andrew[6], M. Angelone[10], C. Angioni[7], I. Antoniou[1], L. Appel[1], C. Appelbee[1], C. Aramunde[1], M. Ariola[4], G. Arnoux[1], G. Artaserse[1,10], J.-F. Artaud[12], W. Arter[1], V. Artigues[7], F.J. Artola[6], A. Ash[1], O. Asztalos[13], D. Auld[1], F. Auriemma[2], Y. Austin[1], L. Avotina[14], J. Ayllón[15], E. Aymerich[16], A. Baciero[17], L. Bähner[18], F. Bairaktaris[19], I. Balboa[1], M. Balden[7], N. Balshaw[1], V.K. Bandaru[7], J. Banks[1], A. Banon Navarro[7], C. Barcellona[20], O. Bardsley[1], M. Barnes[21], R. Barnsley[6], M. Baruzzo[10], M. Bassan[6], A. Batista[3], P. Batistoni[10], L. Baumane[14], B. Bauvir[6], L. Baylor[22], C. Bearcroft[1], P. Beaumont[1], D. Beckett[1], A. Begolli[1], M. Beidler[22], N. Bekris[23], M. Beldishevski[1], E. Belli[24], F. Belli[10], S. Benkadda[25], J. Bentley[1], E. Bernard[12], J. Bernardo[1,3], M. Bernert[7], M. Berry[1], L. Bertalot[6], H. Betar[26], M. Beurskens[7], P.G. Bhat[27], S. Bickerton[1], J. Bielecki[28], T. Biewer[22], R. Bilato[7], P. Bílková[29], G. Birkenmeier[7], R. Bisson[25], J.P.S. Bizarro[3], P. Blatchford[1], A. Bleasdale[1], V. Bobkov[7], A. Boboc[1], A. Bock[7], G. Bodnar[1], P. Bohm[29], L. Bonalumi[30], N. Bonanomi[7], D. Bonfiglio[2], X. Bonnin[6], P. Bonofiglo[31], J. Booth[1], D. Borba[3], D. Borba[32], D. Borodin[33], I. Borodkina[29], T.O.S.J. Bosman[34], C. Bourdelle[12], M. Bowden[1], I. Božičević Mihalić[35], S.C. Bradnam[1], B. Breizman[36], S. Brezinsek[33,37], D. Brida[7], M. Brix[1], P. Brown[1], D. Brunetti[1,5], M. Buckley[1], J. Buermans[38], H. Bufferand[12], P. Buratti[39], A. Burckhart[7], A. Burgess[1], A. Buscarino[20], A. Busse[1], D. Butcher[1], G. Calabrò[40], L. Calacci[39], R. Calado[3], R. Canavan[1], B. Cannas[16], M. Cannon[1], M. Cappelli[10], S. Carcangiu[16], P. Card[1], A. Cardinali[41], S. Carli[42], P. Carman[1], D. Carnevale[39], B. Carvalho[7], I.S. Carvalho[1,3,6], P. Carvalho[1,3], I. Casiraghi[5], F.J. Casson[1], C. Castaldo[10], J.P. Catalan[8], N. Catarino[3], F. Causa[5], M. Cavedon[7,30], M. Cecconello[11], L. Ceelen[34], C.D. Challis[1], B. Chamberlain[1], R. Chandra[43], C.S. Chang[31], A. Chankin[7], B. Chapman[1], P. Chauhan[1], M. Chernyshova[44], A. Chiariello[4], G.-C. Chira[1], P. Chmielewski[44], A. Chomiczewska[44], L. Chone[43], J. Cieslik[1], G. Ciraolo[12], D. Ciric[1], J. Citrin[34], Ł. Ciupinski[45], R. Clarkson[1], M. Cleverly[1], P. Coates[1], V. Coccorese[4], R. Coelho[3], J.W. Coenen[33], I.H. Coffey[46], A. Colangeli[10], L. Colas[12], J. Collins[1], S. Conroy[11], C. Contré[47], N.J. Conway[1], D. Coombs[1], P. Cooper[1], S. Cooper[1], L. Cordaro[2], C. Corradino[20], Y. Corre[12], G. Corrigan[1], D. Coster[7], T. Craciunescu[48], S. Cramp[1], D. Craven[1], R. Craven[1], G. Croci[30], D. Croft[1], K. Crombé[38], T. Cronin[1], N. Cruz[3], A. Cufar[49], A. Cullen[1], A. Dal Molin[5], S. Dalley[1], P. David[7], A. Davies[1], J. Davies[1], S. Davies[1], G. Davis[1], K. Dawson[1], S. Dawson[1], I. Day[1], G. De Tommasi[4], J. Deane[1], M. Dearing[1], M. De Bock[6], J. Decker[47], R. Dejarnac[29], E. Delabie[22], E. de la Cal[17], E. de la Luna[17], D. Del Sarto[26], A. Dempsey[50], W. Deng[1], A. Dennett[1], G.L. Derks[34], G. De Temmerman[6], F. Devasagayam[43], P. de Vries[6], P. Devynck[12], A. di Siena[7]

[*] Author to whom any correspondence should be addressed.

Original content from this work may be used under the terms of the Creative Commons Attribution 4.0 licence. Any further distribution of this work must maintain attribution to the author(s) and the title of the work, journal citation and DOI.

 © 2024 The Author(s). Published by IOP Publishing Ltd on behalf of the IAEA

D. Dickinson[51], T. Dickson[1], M. Diez[12], P. Dinca[48], T. Dittmar[33], L. Dittrich[18], J. Dobrashian[1], T. Dochnal[1], A.J.H. Donné[52], W. Dorland[21], S. Dorling[1], S. Dormido-Canto[53], R. Dotse[1], D. Douai[12,52], S. Dowson[1], R. Doyle[50], M. Dreval[54], P. Drews[33], G. Drummond[1], Ph. Duckworth[6], H.G. Dudding[1,51], R. Dumont[12], P. Dumortier[38], D. Dunai[13], T. Dunatov[35], M. Dunne[7], I. Ďuran[29], F. Durodié[38], R. Dux[7], T. Eade[1], E. Eardley[1], J. Edwards[1], T. Eich[7], A. Eksaeva[33], H. El-Haroun[1], R.D. Ellis[1], G. Ellwood[6], C. Elsmore[1], S. Emery[1], G. Ericsson[11], B. Eriksson[11], F. Eriksson[1], J. Eriksson[11], L.G. Eriksson[55], L.G. Eriksson[56], S. Ertmer[33], G. Evans[1], S. Evans[1], E. Fable[7], D. Fagan[1], M. Faitsch[7], D. Fajardo Jimenez[7], M. Falessi[10], A. Fanni[16], T. Farmer[1], I. Farquhar[1], B. Faugeras[57], S. Fazinić[35], N. Fedorczak[12], K. Felker[58], R. Felton[1], H. Fernandes[3], D.R. Ferreira[3], J. Ferreira[3], G. Ferrò[39], J. Fessey[1], O. Février[47], O. Ficker[29], A.R. Field[1], A. Figueiredo[3], J. Figueiredo[3,52], A. Fil[1], N. Fil[1], P. Finburg[1], U. Fischer[23], G. Fishpool[1], L. Fittill[1], M. Fitzgerald[1], D. Flammini[10], J. Flanagan[1], S. Foley[1], N. Fonnesu[10], M. Fontana[1,47], J.M. Fontdecaba[17], L. Fortuna[20], E. Fortuna-Zalesna[45], M. Fortune[1], C. Fowler[1], P. Fox[1], O. Franklin[1], E. Fransson[55], L. Frassinetti[18], R. Fresa[4], D. Frigione[39], T. Fülöp[59], M. Furseman[1], S. Gabriellini[60], D. Gadariya[17], S. Gadgil[1], K. Gál[52], S. Galeani[39], A. Galkowski[44], D. Gallart[61], M. Gambrioli[62,99], T. Gans[50], J. Garcia[12], M. García-Muñoz[15], L. Garzotti[1], J. Gaspar[62], R. Gatto[60], P. Gaudio[39], D. Gear[1], T. Gebhart[22], S. Gee[1], M. Gelfusa[39], R. George[1], S.N. Gerasimov[1], R. Gerru[63], G. Gervasini[5], M. Gethins[1], Z. Ghani[1], M. Gherendi[48], P.-I. Gherghina[1], F. Ghezzi[5], L. Giacomelli[5], C. Gibson[1], L. Gil[3], M.R. Gilbert[1], A. Gillgren[55], E. Giovannozzi[10], C. Giroud[1], G. Giruzzi[12], J. Goff[1], V. Goloborodko[64], R. Gomes[3], J.-F. Gomez[65], B. Gonçalves[3], M. Goniche[12], J. Gonzalez-Martin[66], A. Goodyear[1], S. Gore[1], G. Gorini[30], T. Görler[7], N. Gotts[1], E. Gow[1], J.P. Graves[47], J. Green[1], H. Greuner[7], E. Grigore[48], F. Griph[1], W. Gromelski[44], M. Groth[43], C. Grove[1], R. Grove[22], N. Gupta[1], S. Hacquin[12,32], L. Hägg[11], A. Hakola[67], M. Halitovs[14], J. Hall[9], C.J. Ham[1], M. Hamed[34], M.R. Hardman[21], Y. Haresawa[1], G. Harrer[68], J.R. Harrison[1], D. Harting[33], D.R. Hatch[36], T. Haupt[1], J. Hawes[1], N.C. Hawkes[1], J. Hawkins[1], S. Hazael[1], J. Hearmon[1], P. Heesterman[1], P. Heinrich[7], M. Held[55], W. Helou[6], O. Hemming[1], S.S. Henderson[1], R. Henriques[1], R.B. Henriques[3], D. Hepple[1], J. Herfindal[22], G. Hermon[1], J.C. Hillesheim[1], K. Hizanidis[19], A. Hjalmarsson[11], A. Ho[34,69], J. Hobirk[7], O. Hoenen[6], C. Hogben[1], A. Hollingsworth[1], S. Hollis[1], E. Hollmann[70], M. Hölzl[7], M. Hook[1], M. Hoppe[47], J. Horáček[29], N. Horsten[42], N. Horsten[43], A. Horton[1], L.D. Horton[32,47], L. Horvath[1], S. Hotchin[1], Z. Hu[30], Z. Huang[1], E. Hubenov[1], A. Huber[33], V. Huber[33], T. Huddleston[1], G.T.A. Huijsmans[6], Y. Husain[1], P. Huynh[12], A. Hynes[1], D. Iglesias[1], M.V. Iliasova[71], M. Imríšek[29], J. Ingleby[1], P. Innocente[2], V. Ioannou-Sougleridis[72], N. Isernia[4], I. Ivanova-Stanik[44], E. Ivings[1], S. Jachmich[6], T. Jackson[1], A.S. Jacobsen[63], P. Jacquet[1], H. Järleblad[73], A. Järvinen[67], F. Jaulmes[29], N. Jayasekera[1], F. Jenko[7], I. Jepu[1,48], E. Joffrin[12], T. Johnson[18], J. Johnston[1], C. Jones[1], E. Jones[1], G. Jones[1], L. Jones[1], T.T.C. Jones[1], A. Joyce[1], M. Juvonen[1], A. Kallenbach[7], P. Kalnina[14], D. Kalupin[52], P. Kanth[1], A. Kantor[1], A. Kappatou[7], O. Kardaun[7], J. Karhunen[1,67], E. Karsakos[1], Ye.O. Kazakov[38], V. Kazantzidis[19], D.L. Keeling[1], W. Kelly[1], M. Kempenaars[6], D. Kennedy[1], K. Khan[1], E. Khilkevich[71], C. Kiefer[7], H.-T. Kim[1], J. Kim[74], S.H. Kim[6], D.B. King[1], D.J. Kinna[1], V.G. Kiptily[1], A. Kirjasuo[67], K.K. Kirov[1], A. Kirschner[33], T. Kiviniemi[43], G. Kizane[14], C. Klepper[22], A. Klix[23], G. Kneale[1], M. Knight[1], P. Knight[1], R. Knights[1], S. Knipe[1], U. Knoche[33], M. Knolker[24], M. Kocan[6], F. Köchl[1], G. Kocsis[1], J.T.W. Koenders[34], Y. Kolesnichenko[64], Y. Kominis[19], M. Kong[1,47], B. Kool[34], V. Korovin[54], S.B. Korsholm[63], B. Kos[49], D. Kos[1], M. Koubiti[25], Y. Kovtun[54], E. Kowalska-Strzęciwilk[44], K. Koziol[75], Y. Krasikov[33], A. Krasilnikov[76], V. Krasilnikov[6], M. Kresina[1,12], A. Kreter[77], K. Krieger[7], A. Krivska[38], U. Kruezi[6], I. Książek[78], H. Kumpulainen[43], B. Kurzan[7], S. Kwak[7], O.J. Kwon[79], B. Labit[47], M. Lacquaniti[16], A. Lagoyannis[72], L. Laguardia[5], A. Laing[1], V. Laksharam[1], N. Lam[1], H.T. Lambertz[33], B. Lane[1], M. Langley[1], E. Lascas Neto[47], E. Łaszyńska[44], K.D. Lawson[1], A. Lazaros[19], E. Lazzaro[5], G. Learoyd[1], C. Lee[80], K. Lee[1], S. Leerink[43], T. Leeson[1], X. Lefebvre[1], H.J. Leggate[50], J. Lehmann[1], M. Lehnen[6], D. Leichtle[23], F. Leipold[6], I. Lengar[49], M. Lennholm[1], E. Leon Gutierrez[17], L.A. Leppin[7], E. Lerche[38], A. Lescinskis[14], S. Lesnoj[1], L. Lewin[1], J. Lewis[1], J. Likonen[67], Ch. Linsmeier[33], X. Litaudon[12], E. Litherland-Smith[1], F. Liu[32], T. Loarer[12], A. Loarte[6], R. Lobel[1], B. Lomanowski[22], P.J. Lomas[1], J. Lombardo[62,99], R. Lorenzini[2], S. Loreti[10], V.P. Loschiavo[4], M. Loughlin[6,22], T. Lowe[1], C. Lowry[1], T. Luce[6], R. Lucock[1], T. Luda Di Cortemiglia[7], M. Lungaroni[39], C.P. Lungu[48], T. Lunt[7], V. Lutsenko[64],

B. Lyons[24], J. Macdonald[1], E. Macusova[29], R. Mäenpää[43], C.F. Maggi[1], H. Maier[7], J. Mailloux[1], S. Makarov[7], P. Manas[12], A. Manning[1], P. Mantica[5], M.J. Mantsinen[81], J. Manyer[61], A. Manzanares[82], Ph. Maquet[6], M. Maraschek[7], G. Marceca[47], G. Marcer[30], C. Marchetto[41], O. Marchuk[33], A. Mariani[5], G. Mariano[10], M. Marin[34,47], A. Marin Roldan[27], M. Marinelli[39], T. Markovič[29], L. Marot[83], C. Marren[1], S. Marsden[1], S. Marsen[7], J. Marsh[1], R. Marshall[1], L. Martellucci[39], A.J. Martin[1], C. Martin[25], R. Martone[4], S. Maruyama[6], M. Maslov[1], M. Mattei[4], G.F. Matthews[1], D. Matveev[33], E. Matveeva[29], A. Mauriya[3], F. Maviglia[4], M. Mayer[7], M.-L. Mayoral[1], S. Mazzi[25], S. Mazzi[47], C. Mazzotta[10], R. McAdams[1], P.J. McCarthy[84], P. McCullen[1], R. McDermott[7], D.C. McDonald[1], D. McGuckin[1], V. McKay[1], L. McNamee[1], A. McShee[1], D. Mederick[1], M. Medland[1], S. Medley[1], K. Meghani[1], A.G. Meigs[1], S. Meitner[22], S. Menmuir[1], K. Mergia[72], S. Mianowski[1], P. Middleton[1], J. Mietelski[28], K. Mikszuta-Michalik[44], D. Milanesio[85], E. Milani[39], E. Militello-Asp[1], F. Militello[1], J. Milnes[1], A. Milocco[30], S. Minucci[40], I. Miron[48], J. Mitchell[1], J. Mlynář[29], J. Mlynář[86], V. Moiseenko[54], P. Monaghan[1], I. Monakhov[1], A. Montisci[16], S. Moon[18], R. Mooney[1], S. Moradi[52], R.B. Morales[1], L. Morgan[1], F. Moro[10], J. Morris[1], T. Mrowetz[1], L. Msero[6], S. Munot[1], A. Muñoz-Perez[15], M. Muraglia[25], A. Murari[2], A. Muraro[5], B. N'Konga[57], Y.S. Na[80], F. Nabais[3], R. Naish[1], F. Napoli[10], E. Nardon[12], V. Naulin[52,63], M.F.F. Nave[3], R. Neu[7], S. Ng[1], M. Nicassio[1], D. Nicolai[33], A.H. Nielsen[63], S.K. Nielsen[63], D. Nina[3], C. Noble[1], C.R. Nobs[1], M. Nocente[30], H. Nordman[6], S. Nowak[5], H. Nyström[18], J. O'Callaghan[1], M. O'Mullane[1], C. O'Neill[1], C. Olde[1], H.J.C. Oliver[1], R. Olney[1], J. Ongena[38], G.P. Orsitto[10], A. Osipov[55], R. Otin[1], N. Pace[1], L.W. Packer[1], E. Pajuste[14], D. Palade[48], J. Palgrave[1], O. Pan[7], N. Panadero[17], T. Pandya[22], E. Panontin[30], A. Papadopoulos[19], G. Papadopoulos[1], G. Papp[7], V.V. Parail[1], A. Parsloe[1], K. Paschalidis[87], M. Passeri[39], A. Patel[1], A. Pau[47], G. Pautasso[7], R. Pavlichenko[54], A. Pavone[7], E. Pawelec[78], C. Paz-Soldan[88], A. Peacock[1], M. Pearce[1], I.J. Pearson[1], E. Peluso[39], C. Penot[6], K. Pepperell[1], A. Perdas[1], T. Pereira[3], E. Perelli Cippo[5], C. Perez von Thun[44], D. Perry[1], P. Petersson[18], G. Petravich[13], N. Petrella[1], M. Peyman[1], L. Pigatto[2], M. Pillon[10], S. Pinches[6], G. Pintsuk[33], C. Piron[10,89,100], A. Pironti[4], F. Pisano[16], R. Pitts[6], U. Planck[7], N. Platt[1], V. Plyusnin[3], M. Podesta[31], G. Pokol[13], F.M. Poli[31], O.G. Pompilian[48], M. Poradzinski[1], M. Porkolab[90], C. Porosnicu[48], G. Poulipoulis[91], A.S. Poulsen[63], I. Predebon[2], A. Previti[10], D. Primetzhofer[11], G. Provatas[35], G. Pucella[10], P. Puglia[1,47], K. Purahoo[1], O. Putignano[30], T. Pütterich[7], A. Quercia[4], G. Radulescu[22], V. Radulovic[49], R. Ragona[63], M. Rainford[1], P. Raj[23], M. Rasinski[33], D. Rasmussen[22], J. Rasmussen[63], J.J. Rasmussen[63], A. Raso[39], G. Rattá[17], S. Ratynskaia[87], R. Rayaprolu[33], M. Rebai[5], A. Redl[40], D. Rees[43], D. Réfy[13], R. Reichle[6], H. Reimerdes[47], B.C.G. Reman[63], C. Reux[12], S. Reynolds[1], D. Rigamonti[5], E. Righi[56], F.G. Rimini[1,52], J. Risner[22], J.F. Rivero-Rodriguez[1,15], C.M. Roach[1], J. Roberts[1], R. Robins[1], S. Robinson[1], D. Robson[1], S. Rode[33], P. Rodrigues[3], P. Rodriguez-Fernandez[90], S. Romanelli[1], J. Romazanov[33], E. Rose[1], C. Rose-Innes[1], R. Rossi[39], S. Rowe[1], D. Rowlands[1], C. Rowley[1], M. Rubel[18], G. Rubinacci[4], G. Rubino[10], M. Rud[63], J. Ruiz Ruiz[21], F. Ryter[7], S. Saarelma[1], A. Sahlberg[11], M. Salewski[63], A. Salmi[67], R. Salmon[1], F. Salzedas[3,92], F. Sanchez[83], I. Sanders[1], D. Sandiford[1], F. Sanni[1], O. Sauter[47], P. Sauvan[8], G. Schettini[93], A. Shevelev[71], A.A. Schekochihin[21], K. Schmid[7], B.S. Schmidt[63], S. Schmuck[5], M. Schneider[6], P.A. Schneider[7], N. Schoonheere[12], R. Schramm[7], D. Scoon[1], S. Scully[1], M. Segato[1], J. Seidl[29], L. Senni[10], J. Seo[80], G. Sergienko[33], M. Sertoli[1], S.E. Sharapov[1], R. Sharma[1], A. Shaw[1], R. Shaw[1], H. Sheikh[1], U. Sheikh[47], N. Shi[24], P. Shigin[6], D. Shiraki[22], G. Sias[16], M. Siccinio[7], B. Sieglin[7], S.A. Silburn[1], A. Silva[3], C. Silva[3], J. Silva[1], D. Silvagni[7], D. Simfukwe[1], J. Simpson[1,43], P. Sirén[1,94], A. Sirinelli[6], H. Sjöstrand[11], N. Skinner[1], J. Slater[1], T. Smart[1], R.D. Smirnov[70], N. Smith[1], P. Smith[1], T. Smith[1], J. Snell[1], L. Snoj[49], E.R. Solano[17], V. Solokha[43], C. Sommariva[47], K. Soni[83], M. Sos[29], J. Sousa[3], C. Sozzi[5], T. Spelzini[1], F. Spineanu[48], L. Spolladore[39], D. Spong[22], C. Srinivasan[1], G. Staebler[24], A. Stagni[62,99], I. Stamatelatos[72], M.F. Stamp[1], Ž. Štancar[1], P.A. Staniec[1], G. Stankūnas[95], M. Stead[1], B. Stein-Lubrano[90], A. Stephen[1], J. Stephens[1], P. Stevenson[1], C. Steventon[1], M. Stojanov[1], D.A. St-Onge[21], P. Strand[55], S. Strikwerda[1], C.I. Stuart[1], S. Sturgeon[1], H.J. Sun[1], S. Surendran[1], W. Suttrop[7], J. Svensson[7], J. Svoboda[29], R. Sweeney[90], G. Szepesi[1], M. Szoke[1], T. Tadić[35], B. Tal[7], T. Tala[67], P. Tamain[12], K. Tanaka[96], W. Tang[31], G. Tardini[7], M. Tardocchi[5], D. Taylor[1], A.S. Teimane[14], G. Telesca[44], A. Teplukhina[31], A. Terra[33], D. Terranova[2], N. Terranova[10], D. Testa[47], B. Thomas[1],

V.K. Thompson[1], A. Thorman[1], A.S. Thrysoe[63], W. Tierens[7], R.A. Tinguely[90], A. Tipton[1], H. Todd[1], M. Tomeš[29], A. Tookey[1], P. Tsavalas[72], D. Tskhakaya[29], L.-P. Turică[21], A. Turner[1], I. Turner[1], M. Turner[1], M.M. Turner[50], G. Tvalashvili[1], A. Tykhyy[64], S. Tyrrell[1], A. Uccello[5], V. Udintsev[6], A. Vadgama[1], D.F. Valcarcel[1], A. Valentini[63], M. Valisa[2], M. Vallar[47], M. Valovic[1], M. Van Berkel[34], K.L. van de Plassche[34], M. van Rossem[47], D. Van Eester[38], J. Varela[97], J. Varje[43], T. Vasilopoulou[72], G. Vayakis[6], M. Vecsei[13], J. Vega[17], M. Veis[27], P. Veis[27], S. Ventre[4], M. Veranda[2], G. Verdoolaege[9], C. Verona[39], G. Verona Rinati[39], E. Veshchev[6], N. Vianello[2], E. Viezzer[15], L. Vignitchouk[87], R. Vila[17], R. Villari[10], F. Villone[4], P. Vincenzi[2], A. Vitins[14], Z. Vizvary[1], M. Vlad[48], I. Voldiner[17], U. Von Toussaint[7], P. Vondráček[29], B. Wakeling[1], M. Walker[1], R. Walker[1], M. Walsh[6], R. Walton[1], E. Wang[33], F. Warren[1], R. Warren[1], J. Waterhouse[1], C. Watts[6], T. Webster[1], M. Weiland[7], H. Weisen[47,98], M. Weiszflog[11], N. Wendler[44], A. West[1], M. Wheatley[1], S. Whetham[1], A. Whitehead[1], D. Whittaker[1], A. Widdowson[1], S. Wiesen[33], M. Willensdorfer[7], J. Williams[1], I. Wilson[1], T. Wilson[1], M. Wischmeier[7], A. Withycombe[1], D. Witts[1], A. Wojcik-Gargula[28], E. Wolfrum[7], R. Wood[1], R. Woodley[1], R. Worrall[1], I. Wyss[39], T. Xu[1], D. Yadykin[55], Y. Yakovenko[64], Y. Yang[6], V. Yanovskiy[29], R. Yi[33], I. Young[1], R. Young[1], B. Zaar[18], R.J. Zabolockis[14], L. Zakharov[94], P. Zanca[2], A. Zarins[14], D. Zarzoso Fernandez[25], K.-D. Zastrow[1], Y. Zayachuk[1], M. Zerbini[10], W. Zhang[7], B. Zimmermann[7], M. Zlobinski[33], A. Zocco[7], V.K. Zotta[60], M. Zuin[2], W. Zwingmann[3] and I. Zychor[75]

[1] United Kingdom Atomic Energy Authority, Culham Campus, Abingdon, Oxfordshire OX14 3DB, United Kingdom of Great Britain and Northern Ireland
[2] Consorzio RFX (CNR, ENEA, INFN, Università di Padova, Acciaierie Venete SpA), C.so Stati Uniti 4, 35127 Padova, Italy
[3] Instituto de Plasmas e Fusão Nuclear, Instituto Superior Técnico, Universidade de Lisboa, 1049-001 Lisboa, Portugal
[4] Consorzio CREATE, Via Claudio 21, 80125 Napoli, Italy
[5] Institute for Plasma Science and Technology, CNR, via R. Cozzi 53, 20125 Milano, Italy
[6] ITER Organization, Route de Vinon-sur-Verdon, CS 90 046, 13067 Saint Paul Lez Durance Cedex, France
[7] Max-Planck-Institut für Plasmaphysik, D-85748 Garching, Germany
[8] Dept Ingn Energet, Universidad Nacional de Educacion a Distancia, Calle Juan del Rosal 12, E-28040 Madrid, Spain
[9] Department of Applied Physics, Ghent University, 9000 Ghent, Belgium
[10] Dip.to Fusione e Tecnologie per la Sicurezza Nucleare, ENEA C. R. Frascati, via E. Fermi 45, 00044 Frascati (Roma), Italy
[11] Department of Physics and Astronomy, Uppsala University, SE-75120 Uppsala, Sweden
[12] CEA, IRFM, F-13108 Saint Paul Lez Durance, France
[13] Centre for Energy Research, POB 49, H-1525 Budapest, Hungary
[14] University of Latvia, 19 Raina Blvd., Riga, LV 1586, Latvia
[15] Universidad de Sevilla, Sevilla, Spain
[16] Department of Electrical and Electronic Engineering, University of Cagliari, Piazza d'Armi 09123 Cagliari, Italy
[17] Laboratorio Nacional de Fusión, CIEMAT, Madrid, Spain
[18] Fusion Plasma Physics, EECS, KTH Royal Institute of Technology, SE-10044 Stockholm, Sweden
[19] National Technical University of Athens, Iroon Politechniou 9, 157 73 Zografou, Athens, Greece
[20] Dipartimento di Ingegneria Elettrica Elettronica e Informatica, Università degli Studi di Catania, 95125 Catania, Italy
[21] Rudolf Peierls Centre for Theoretical Physics, University of Oxford, Oxford OX1 3PU, United Kingdom of Great Britain and Northern Ireland
[22] Oak Ridge National Laboratory, Oak Ridge, TN 37831, United States of America
[23] Karlsruhe Institute of Technology, PO Box 3640, D-76021 Karlsruhe, Germany
[24] General Atomics, PO Box 85608, San Diego, CA 92186-5608, United States of America
[25] Aix-Marseille University, CNRS, PIIM, UMR 7345, 13013 Marseille, France
[26] Universite´de Lorraine, CNRS, IJL, F-54000 Nancy, France
[27] Faculty of Mathematics, Department of Experimental Physics, Physics and Informatics Comenius University, Mlynska dolina F2, 84248 Bratislava, Slovakia

[28] Institute of Nuclear Physics, Radzikowskiego 152, 31-342 Kraków, Poland
[29] Institute of Plasma Physics of the CAS, Za Slovankou 1782/3, 182 00 Praha 8, Czech Republic
[30] University of Milano-Bicocca, Piazza della Scienza 3, 20126 Milano, Italy
[31] Princeton Plasma Physics Laboratory, James Forrestal Campus, Princeton, NJ 08543, United States of America
[32] EUROfusion Programme Management Unit, Culham Science Centre, Culham OX14 3DB, United Kingdom of Great Britain and Northern Ireland
[33] Forschungszentrum Jülich GmbH, Institut für Energie- und Klimaforschung, Plasmaphysik, 52425 Jülich, Germany
[34] FOM Institute DIFFER, Eindhoven, Netherlands
[35] Ruđer Bošković Institute, Bijenička 54, 10000 Zagreb, Croatia
[36] University of Texas at Austin, Institute for Fusion Studies, Austin, TX 78712, United States of America
[37] Heinrich-Heine-Universität Düsseldorf, 40225 Düsseldorf, Germany
[38] Laboratory for Plasma Physics LPP-ERM/KMS, B-1000 Brussels, Belgium
[39] Università di Roma Tor Vergata, Via del Politecnico 1, Roma, Italy
[40] University of Tuscia, DEIM, Via del Paradiso 47, 01100 Viterbo, Italy
[41] Istituto dei Sistemi Complessi—CNR and Dipartimento di Energia—Politecnico di Torino, C.so Duca degli Abruzzi 24, 10129 Torino, Italy
[42] Toegepaste Mechanica en Energieconversie, Katholieke Universiteit of Leuven, 3001 Leuven, Belgium
[43] Aalto University, PO Box 14100, FIN-00076 Aalto, Finland
[44] Institute of Plasma Physics and Laser Microfusion, Hery 23, 01-497 Warsaw, Poland
[45] Warsaw University of Technology, 02-507 Warsaw, Poland
[46] Astrophysics Research Centre, School of Mathematics and Physics, Queen's University, Belfast BT7 1NN, United Kingdom of Great Britain and Northern Ireland
[47] Ecole Polytechnique Fédérale de Lausanne (EPFL), Swiss Plasma Center (SPC), CH-1015 Lausanne, Switzerland
[48] The National Institute for Laser, Plasma and Radiation Physics, Magurele-Bucharest, Romania
[49] Slovenian Fusion Association (SFA), Jozef Stefan Institute, Jamova 39, SI-1000 Ljubljana, Slovenia
[50] Dublin City University (DCU), Dublin, Ireland
[51] York Plasma Institute, Department of Physics, University of York, Heslington, York YO10 5DD, United Kingdom of Great Britain and Northern Ireland
[52] EUROfusion Programme Management Unit, Boltzmannstr. 2, 85748 Garching, Germany
[53] UNED, Dpto. Informática y Automática, Madrid, Spain
[54] National Science Center 'Kharkov Institute of Physics and Technology', Akademichna 1, Kharkiv 61108, Ukraine
[55] Department of Space, Earth and Environment, Chalmers University of Technology, SE-41296 Gothenburg, Sweden
[56] European Commission, B-1049 Brussels, Belgium
[57] Université Cote d'Azur, CNRS, Inria, LJAD, Parc Valrose, 06108 Nice Cedex 02, France
[58] Argonne National Laboratory, Lemont, IL 60439, United States of America
[59] Department of Physics, Chalmers University of Technology, SE-41296 Gothenburg, Sweden
[60] Dipartimento di Ingegneria Astronautica, Elettrica ed Energetica, SAPIENZA Università di Roma, Via Eudossiana 18, 00184 Roma, Italy
[61] Barcelona Supercomputing Center, Barcelona, Spain
[62] Aix-Marseille University, CNRS, IUSTI, UMR 7343, 13013 Marseille, France
[63] Department of Physics, Technical University of Denmark, Bldg 309, DK-2800 Kgs Lyngby, Denmark
[64] Institute for Nuclear Research, Prospekt Nauky 47, Kyiv 03680, Ukraine
[65] Harvard University, Harvard Square, Cambridge, MA 02138, United States of America
[66] University of California, Irvine, CA 92697, United States of America
[67] VTT Technical Research Centre of Finland, PO Box 1000, FIN-02044 VTT, Finland
[68] Technische Universität Wien, Fusion@ÖAW Österreichische Akademie der Wissenschaften (ÖAW), Austria
[69] Eindhoven University of Technology, Eindhoven, Netherlands
[70] University of California at San Diego, La Jolla, CA 92093, United States of America
[71] Ioffe Physico-Technical Institute, 26 Politekhnicheskaya, St Petersburg 194021, Russian Federation
[72] NCSR 'Demokritos', 153 10, Agia Paraskevi Attikis, Greece
[73] Department of Applied Mathematics and Computer Science, Technical University of Denmark, Bldg 309, DK-2800 Kgs Lyngby, Denmark
[74] Korea Institute of Fusion Energy, Daejeon, Korea, Republic Of
[75] National Centre for Nuclear Research (NCBJ), 05-400 Otwock-Świerk, Poland
[76] Institution 'Project Center ITER', Moscow 123182, Russian Federation
[77] Jülich GmbH, Institut für Energie- und Klimaforschung, Plasmaphysik, 52425 Jülich, Germany
[78] Institute of Physics, Opole University, Oleska 48, 45-052 Opole, Poland

[79] Daegu University, Jillyang, Gyeongsan, Gyeongbuk 712-174, Korea, Republic Of
[80] Department of Nuclear Engineering, Seoul National University, Seoul, Korea, Republic Of
[81] ICREA and Barcelona Supercomputing Center, Barcelona, Spain
[82] Universidad Complutense de Madrid, Madrid, Spain
[83] Department of Physics, University of Basel, Switzerland
[84] University College Cork (UCC), Cork, Ireland
[85] Politecnico di Torino, Corso Duca degli Abruzzi 24, I-10129 Torino, Italy
[86] Faculty of Nuclear Sciences and Physical Engineering, Czech Technical University in Prague, Břehová 78/7, 115 19 Praha 1, Czech Republic
[87] Space and Plasma Physics, EECS, KTH SE-100 44 Stockholm, Sweden
[88] Columbia University, New York, NY 10027, United States of America
[89] Consorzio RFX, Corso Stati Uniti 4, 35127 Padova, Italy
[90] MIT Plasma Science and Fusion Center, Cambridge, MA 02139, United States of America
[91] University of Ioannina, Panepistimioupoli Ioanninon, PO Box 1186, 45110 Ioannina, Greece
[92] Universidade do Porto, Faculdade de Engenharia, 4200-465 Porto, Portugal
[93] University Roma Tre, via Vito Volterra N°62, CAP 00146 Rome, Italy
[94] University of Helsinki, PO Box 43, FI-00014 Helsinki, Finland
[95] Lithuanian Energy Institute, Breslaujos g. 3, LT-44403 Kaunas, Lithuania
[96] National Institute for Fusion Science, Oroshi, Toki, Gifu 509-5292, Japan
[97] Universidad Carlos III de Madrid, 28911 Leganes, Madrid, Spain
[98] V.N. Karazin Kharkiv National University, Kharkiv, Ukraine
[99] CRF—University of Padova, 35127 Padova, Italy
[100] Dipartimento di Fisica 'G. Galilei', Universita' degli Studi di Padova, Padova, Italy

E-mail: Costanza.Maggi@ukaea.uk

Received 23 November 2023, revised 1 April 2024
Accepted for publication 12 April 2024
Published 28 August 2024

Abstract

In 2021 JET exploited its unique capabilities to operate with T and D–T fuel with an ITER-like Be/W wall (JET-ILW). This second major JET D–T campaign (DTE2), after DTE1 in 1997, represented the culmination of a series of JET enhancements—new fusion diagnostics, new T injection capabilities, refurbishment of the T plant, increased auxiliary heating, in-vessel calibration of 14 MeV neutron yield monitors—as well as significant advances in plasma theory and modelling in the fusion community. DTE2 was complemented by a sequence of isotope physics campaigns encompassing operation in pure tritium at high T-NBI power. Carefully conducted for safe operation with tritium, the new T and D–T experiments used 1 kg of T (vs 100 g in DTE1), yielding the most fusion reactor relevant D–T plasmas to date and expanding our understanding of isotopes and D–T mixture physics. Furthermore, since the JET T and DTE2 campaigns occurred almost 25 years after the last major D–T tokamak experiment, it was also a strategic goal of the European fusion programme to refresh operational experience of a nuclear tokamak to prepare staff for ITER operation. The key physics results of the JET T and DTE2 experiments, carried out within the EUROfusion JET1 work package, are reported in this paper. Progress in the technological exploitation of JET D–T operations, development and validation of nuclear codes, neutronic tools and techniques for ITER operations carried out by EUROfusion (started within the Horizon 2020 Framework Programme and continuing under the Horizon Europe FP) are reported in (Litaudon *et al Nucl. Fusion* accepted), while JET experience on T and D–T operations is presented in (King *et al Nucl. Fusion* submitted).

Keywords: magnetic fusion, JET-ILW, D–T, tritium, alpha particles, fusion prediction, heat and particle transport

(Some figures may appear in colour only in the online journal)

1. Introduction

Tokamak experiments using the D–T mixtures required in fusion power plants are very rare, as magnetic confinement fusion experiments typically use a single hydrogen isotope, primarily deuterium. The JET tokamak was designed from the start to operate with T and D–T fuel. A Preliminary Tritium Experiment (PTE) was carried out in 1991: a hot-ion H-mode plasma with 11% tritium in deuterium produced 2 MJ of fusion energy with peak D–T fusion power $P_{\rm fus} = 1.7$ MW and $Q_{\rm in} = P_{\rm fus}/P_{\rm in} = 0.12$ [1], where $P_{\rm in}$ is the total input power injected into the torus. For the PTE, tritium and neutron budgets were kept low on purpose to limit vessel activation and thus allow the subsequent installation of the JET pumped divertor with human intervention. The first major D–T experiment on JET (DTE1) was carried out in 1997 [2, 3], yielding record D–T fusion power of 16.1 MW in an ELM-free hot-ion H-mode and record 22 MJ fusion energy in a steady, high plasma current type I ELMy H-mode. In 2003, a trace T experiment was carried out in JET [4]. Extensive D–T experiments were also carried out in TFTR between 1993 and 1997 [5–8], with various D–T mixtures, including 50–50 D–T. They produced 10.7 MW of fusion power and fusion gain $Q_{\rm in} = 0.27$ in the supershot regime. Until DTE2, carried out on JET with Be/W wall in 2021, these were the only experiments to date providing nuclear tokamak operation. They demonstrated D–T fusion production, plasma physics effects linked to the use of D–T mixtures and effects linked to the generation of fusion-born α-particles. However, these D–T experiments were primarily carried out in conditions less relevant to ITER and DEMO and fusion power plants, namely with C wall (showing unacceptably high T retention [9] in view of a reactor, both on safety and fuel cycle economics grounds), mostly in transient plasma scenarios (hot-ion H-mode, super shot) in conditions of low density and $T_{\rm i} \gg T_{\rm e}$. Only one scenario, the JET DTE1 sustained type I ELMy H-mode at high plasma current, was carried out in ITER-relevant scenario, but was operated at $\beta_{\rm N} \sim 1.5$ due to limitations in the maximum auxiliary heating, thus sustained fusion power was not obtained in high beta, high fusion power plasmas. Furthermore, especially in JET, α-particle effects were difficult to unravel and isotope effects on transport and confinement on JET were at variance with TFTR results. For DTE1, key diagnostics were either missing, such as H-mode pedestal profiles measurements, or not as advanced as nowadays.

Plans for a second major JET D–T campaign, DTE2, already started in 2006 to test crucial physics and technology aspects of reactor-relevant D–T fusion plasmas ahead of ITER's operations. JET's carbon wall was replaced in 2009–2011 by the ITER-like combination of Be in the main chamber and W in the divertor. Furthermore, a full T campaign at high power would address issues of isotopic effects on particle, energy and momentum transport and plasma-wall interactions, which had remained largely unexplored since the TFTR and JET D–T experiments in the 1990s. As α-particle effects had been weak and difficult to understand in DTE1, in DTE2 emphasis was also placed on demonstrating unambiguous α-particle effects.

Following the installation of the metallic wall [10], a decade of JET experiments, analyses and modelling confirmed the reduced hydrogen fuel retention rate in the Be/W wall (2011–2014) [11], demonstrated in D plasmas the compatibility of ITER scenarios with the ITER-like wall (2016–2020) [12] and investigated a large breadth of isotope physics issues in dedicated H, D, T, and H–D, H–T campaigns (2016–2021). In support of the T and DTE2 experiments, a series of JET enhancements were completed over the years [12, 13], notably: new fusion diagnostics, new T injection capabilities, refurbishment of the T plant, increased auxiliary heating, in-vessel calibration of 14 MeV neutron yield monitors. Significant advances in plasma theory and modelling were accomplished in the fusion community since DTE1. The JET T and D–T experiments were guided by intense 'predict-first' modelling using different codes and modelling assumptions [14]. After DTE2, intensive validation of a variety of core integrated modelling workflows was carried out against the 2021 JET D–T data to test and improve D–T predictive modelling capability for ITER and future fusion reactors [15]. Indeed, the most significant output of DTE2 is the validation of current models and physics workflows in the most D–T fusion reactor relevant conditions to date.

2. Scope of T and DTE2 experiments, upgrades for and operation in T and DTE2

The JET T and DTE2 experiments with Be/W wall were planned and executed along six main goals:

(i) Demonstrate fusion power $\geqslant$10 MW, sustained for 5 s
(ii) Demonstrate an ITER-relevant, Ne-seeded radiative scenario in D–T with the Be/W wall
(iii) Demonstrate clear α-particle effects
(iv) Clarify isotope effects on energy and particle transport and explore consequences of mixed species plasma
(v) Address key plasma–wall interaction issues
(vi) Demonstrate radio-frequency heating schemes relevant to ITER D–T operation.

The scope of T and D–T experiments in JET with Be/W wall was thus much greater than in DTE1. To match this broader scope, both tritium and 14 MeV neutron budgets available for the T and DTE2 campaigns were much larger than in DTE1: the 14 MeV neutron budget was 1.55×10^{21} for DTE2 (vs 2.5×10^{20} in DTE1) and 1×10^{20} for the full T campaign (based on a conservative estimate of 1% D/(D + T) in T plasmas). We recall that the JET safety case defines the limit on the vessel activation due to the total 14 MeV neutron fluence over the lifetime of JET (2×10^{21} 14 MeV neutrons) [16, 17]. The DTE2 neutron budget implied no human access to the tokamak vessel and significant limitations of access ex-vessel in the torus hall for several months after the experiment due to

the high activation levels. A total 8.5×10^{20} neutrons were produced in DTE2, thus allowing for further DTE3 experiments in late 2023. The on-site tritium inventory at the start of the T and D–T campaigns was 69 g, compared to 21 g in DTE1. Overall, 1 kg of T was used for the T and DTE2 campaigns combined (compared to ∼100 g T used in DTE1), of which 240 g were injected into plasma via the tritium gas injection modules (TIMs) [18] and 763 g were fed to the NBI system. In DTE1, with a shorter campaign, 65 g T went to the NBI and 35 g into the vessel. Whereas in DTE1 tritium was fed to the torus by only one midplane TIM, enhanced capability was put in place for T and DTE2, with 5 TIMs installed in different toroidal and poloidal locations of the vessel [18], substantially increasing the T fuelling flexibility. Furthermore, tritium was fed into both neutral beam injection boxes to allow for T experiments at full power, while only one NBI box was converted to T in DTE1.

While the NBI system could supply 20.5 MW in D and up to 23 MW in D–T during DTE1, the subsequent JET NBI upgrades allowed for up to 30 MW peak NB power in T and D–T and up to 26 MW and 29 MW averaged over 3 s in T and DTE2, respectively. Evaluation and calibration of the power from tritium neutral beam injection was also achieved: a combination of operator activities on the NBI system and L-mode plasma experiments comparing the plasma stored energy response for D and T NBI established that the uncertainty in NBI power calibration is comparable in D and T (∼±10%) [19]. The ICRH power available for T and DTE2 was lower than maximum capability due to the unavailability of the ILA antenna. Up to 4–5 MW of RF heating were coupled to plasma, the exact power levels depending on the RF heating scheme and frequency used in the experiments [20].

The Active Gas Handling System (AGHS) [21], the part of the JET plant which stores, supplies and recycles tritium fed to and exhausted from the JET vessel and the NBI, was enhanced and re-commissioned for the T and DTE2 experiments, as it had not been operated since 2003. Tritium was stored in uranium beds and reprocessed in the AGHS to high purity by gas chromatography. To meet the demands of the experimental schedule, the AGHS was operated 24 h a day, 7 d a week. During experimental days, the AGHS provided daily tritium feed to torus and NBI, daily gas exhaust recovery and overnight storage. T and D–T operations were run in cycles, interleaving 3–4 weeks of experiments with one week (without experiments) for legally required T accountancy. During T and DTE2 campaigns, JET operations were restricted by a daily limit of 11 g (44 bar-l) of tritium on the inventory allowed in torus and cryo-panels (divertor and neutral beams), as set by the JET D–T safety case. An overall limit of 90 bar-l hydrogen (all isotopes) per day could be processed by AGHS. The cryo-panels were regenerated at the end of each experimental day or when the daily limit of 11 g T was reached.

To maximize return on investment for DTE2, an in-vessel calibration of the JET 14 MeV neutron yield monitors (three pairs of ^{235}U/^{238}U fission chambers mounted close to the transformer magnet limbs in octants 2, 6 and 8 of the tokamak and an in-vessel activation system, with a reference irradiation end located in octant 3 of the tokamak) was carried out in 2017 with a calibrated 14 MeV neutron generator [22] deployed by remote handling inside the JET vacuum vessel [23]. A total of 76 h of irradiation were needed with the neutron generator located in 73 different poloidal and toroidal positions in the JET vessel to calibrate the JET 14 MeV neutron yield monitors. The 14 MeV neutron generator had been well characterized and absolutely calibrated in advance. It had been equipped with calibrated monitoring detectors, which provided the instantaneous neutron emission rate with ±3.5% uncertainty [22]. Subsequently, the neutron calibration factors for D–T plasmas were derived from measurements of the response function of JET neutron monitors with required corrections provided by neutronics analyses [23]. In particular, the neutronics calculations were performed with the MCNP code and a detailed model of JET to obtain the response of the JET neutron detectors to D–T plasma neutrons starting from the response to the 14 MeV neutron generator neutrons, taking into account the anisotropy of the neutron generator and all the calibration circumstances [23]. In addition to deriving calibration factors for the reference fission chambers, the in-vessel calibration served to validate the neutronics models of the irradiation end located closest to the plasma, which enabled an additional integral measure of fusion yield to be determined.

This calibration method, developed on JET, also benchmarked the ITER neutron calibration workflow, which requires an accuracy of ±10% for T accountancy purposes besides for fusion yield measurements. The final validation of the JET 14 MeV neutron calibration, and its uncertainty quantification, was obtained with measurements of neutron yields during DTE2. Absolute integral fusion neutron yields were determined during the DTE2 campaign using the neutron activation system, using a set of standard high-threshold dosimetry foils (iron, aluminium and niobium), which were routinely irradiated during plasma discharges. The activity induced in these foils directly correlates to the fusion power. To take into account the variable plasma position during discharges, correction factors were derived from dedicated shots during DTE2, in which the plasma was scanned at various heights (Z) above the midplane. These derived correction factors apply to activation coefficients derived from neutronics models, which assume the plasma to be at a given (fixed) height above the midplane. Coupling the γ-spectrometry analysis with neutronics simulations and pre-determined plasma vertical displacement corrections factors allows one to accurately determine the absolute fusion power for any given shot.

Thus, two methods were employed to determine fusion power during the DTE2 campaign, activation foils and absolutely calibrated fission chambers. Both sets of results agreed within the target uncertainty (<10%) and pave the way for a similar methodology to be deployed on ITER.

Further unique opportunities for neutronics included the installation of samples to study 14 MeV neutron induced activation and damage in ITER materials; validation of neutron streaming modelling and of ITER shutdown dose rates; extensive neutronics measurements in a wide range of plasma scenarios and in JET non-operational periods [24]. For reference, the neutron flux levels measured at the JET first wall were of the same order of magnitude of those expected at the rear

ITER blanket/diagnostic first wall for ITER $Q = 10$ operation and the γ-radiation field in JET due to neutron activation after DTE2 was as intense as that expected in maintenance locations of ITER [24].

Measurements enhancements for DTE2 in the area of nuclear diagnostics for fusion products, which are crucial to test D–T modelling predictions with high level of detail, included: neutron spectroscopy, with two main instruments used, the magnetic proton coil spectrometer (MPRu) [25], used in DTE1 and upgraded for DTE2, and new crystal, synthetic diamond detectors; measurements of lost fast ions, in particular α-particles, with a fast ion loss detector (FILD) for measurement of the velocity space of the escaping α-particles, and an array of five Faraday cups, which yield information on the poloidal distribution of the losses [26, 27].

The power and energy handling limits of JET's Be/W wall are such that the surface temperature of the Be limiters needs to be kept below 900 °C to avoid melting and the tungsten-coated CFC tiles in the divertor (except the bulk W tile) have a surface temperature limit of 1200 °C to avoid carbidisation of the coating and brittle failure. A significant upgrade of the JET machine protection and control system (consisting of an array of pyrometers, infra-red cameras and a suite of real-time vessel temperature monitoring and alarm generation software) was thus put in place, including an in-vessel calibration of the sensors in 2017. A key diagnostic upgrade in preparation for DTE2 was the installation of remote optical links to bring two of the in-vessel views outside the biological shield of the machine, to ensure their use for machine protection and physics applications during the high fusion pulses in DTE2 [28, 29]. Cameras close coupled to the machine were removed prior to DTE2 to preserve their electronics, which would otherwise have been damaged by the high neutron and γ-ray emission. The cameras were then re-installed, when access to the torus hall was allowed again, for the subsequent D campaigns in 2022 and 2023.

In this paper, unless otherwise stated, the quoted hydrogen isotopic composition is that measured by high resolution H, D, T Balmer-α spectroscopy of a Penning discharge within the neutral gas analysis diagnostic in the JET sub-divertor plenum [30]. Light is collected from a Penning gauge and fed into quartz optic fibres which relay the light to the JET diagnostic hall. The light is analysed with a high-resolution visible spectrometer which uses a CCD camera as detector. The optical Penning gauges and associated spectroscopic instrumentation were upgraded prior to DTE2 to provide improved optical throughput and, for the first time, simultaneous routine measurement of H/D/T and ^{3}He/^{4}He ratios. As the JET multi-sensor neutral gas analysis diagnostic shares many design features with the neutral gas analysis system on ITER, this is one of the many examples where DTE2 also provided an excellent testbed for the ITER measurement workflow [31]. The isotopic concentration detection limit is 1% [30, 32]. The ability to measure T and D concentrations of 1% or below was particularly important in D and T campaigns, respectively, prior to and after DTE2, as the 14 MeV neutron budget was strictly monitored for optimum use during DTE2. It is to note that accurate detection of low-level concentrations of D and/or T in plasmas that include both isotopes is more challenging than extracting H concentrations in either D or T, as the D_α and T_α spectral lines are much closer to each other.

Another key diagnostic upgrade for the T and D–T experiments in JET-ILW was that of the core charge exchange recombination spectroscopy (CXRS) system, which allowed recovering high quality ion temperature (T_i) and toroidal rotation (v_{tor}) profiles with the Be/W wall, where C impurity content in the plasma is negligibly low [33]. T_i and v_{tor} profiles were typically measured by Ne X CXRS, enabled by diagnostic Ne puffs. Main ion core CXRS was also implemented as part of this upgrade.

A transition from deuterium to protium operation was programmed at the end of 2020, in order to minimize the deuterium concentration in plasma and, therefore, the 14 MeV neutron yields during the experiments in pure T, while also providing the final H references for isotope physics studies. This was followed by the physics programme in T and D–T, which entailed in sequence: a full tritium campaign, including high power T operation; experiments in deuterium–tritium mixtures (DTE2); completion of the T campaign in early 2022. Subsequently, a clean-up phase in hydrogen and low-power D plasmas was executed to ensure tritium removal from the vessel (see section 7). An overview of the key results from the JET T and DTE2 experiments with Be/W wall is reported in sections 3–8, organized along the six campaigns headlines, and conclusions are drawn in section 9.

3. Demonstration of high fusion power, sustained for 5 s

Prior to DTE2, the most reactor-relevant D–T plasmas of current generation tokamaks were achieved in JET DTE1. In particular, $P_{fus} \sim 4$ MW was obtained in a high power, type I ELMy H-mode steady for 5 s, with pulse duration limited by the duration of the auxiliary heating phase at maximum power and the available neutron budget [34]. This plasma, pulse #42982, 50–50 D–T, 3.8 MA/3.8 T, $q_{95} = 3.5$, 21.5 MW NBI + 2.3 MW ICRH, performed with the JET Mark IIA divertor and C-wall, set the world record of 22 MJ of fusion energy, with $Q_E = 0.18$ (defined as the fusion energy produced over the input energy into plasma over the 5 s steady time interval). The thermal neutron yield reached ~30% of the total neutron yield. All other DTE1 high performance scenarios (hot ion ELM-free H-mode, reversed shear H-mode with internal transport barrier (ITB)), although yielding significantly higher peak P_{fus} values [2], were highly transient.

In JET DTE2, high D–T fusion performance of ELMy H-modes was sought at maximum plant capability, within neutron and T budgets allocated to the entire campaign, with emphasis on sustained performance compatible with the Be/W wall: maximum auxiliary heating in plasmas sustained for 5 s (with this duration limited by the thermal inertia and between pulse cooling of the tokamak's wall and copper magnetic coils), namely ~25 τ_E's. In doing so, JET was pushed to operate at its operational limits while remaining compatible with the constraints of the metallic wall, demonstrating

maximum D–T fusion performance steady over several energy confinement times and α-particle slowing down times. Thus, the primary goal of DTE2 was not to achieve a given value of fusion power or energy, but, rather, to demonstrate integrated fusion performance in conditions as close as possible to those in ITER, while aiming at sustained fusion powers approaching those of the record $P_{\rm fus}$ achieved only transiently in DTE1.

Preparation of the scenarii for high $P_{\rm fus}$ was completed in 2019–2020 [12], delivering record sustained neutron rates in D in the hybrid scenario, up to 3.3×10^{16} n s^{-1} (averaged over 5 s), with tolerable (for JET-ILW) divertor heat loads and medium/high-Z impurity control for steady H-mode operation. As earlier studies with JET-ILW highlighted the sensitivity of ELM frequency and pedestal pressure to gas injection [35], it was a general need of all scenarii to optimize this aspect for high fusion performance with high-Z impurity control. Extrapolation from D to D–T with predictive modelling and/or with D–T equivalent fusion power calculations indicated that 10 MW of fusion power or more could be delivered, with values depending on the modelling assumptions and the nominal auxiliary heating used in the simulations [14]. Two complementary routes were pursued to test different D–T physics and fusion drives with a Be/W wall: high current (baseline scenario) and high beta (hybrid scenario).

The baseline and hybrid scenarii were developed with 50–50 D–T plasma mixtures over the entire plasma radius using mixed D–T core (via NBI) and edge (via TIMs) fuelling to maximize the thermonuclear reactivity and thus approach as much as possible on JET the burning conditions of ITER and DEMO and other future fusion reactors. In JET D–T plasmas, for typical core $T_{\rm i} \sim 10$ keV, the fusion power always has a significant contribution driven by non-thermal fusion reactions, primarily 'beam-target' reactions between fast ions from the NBI heating (injected at ∼100–120 keV on JET, close to the maximum D–T cross section, see e.g. [36]) and thermal bulk ions, since NBI heating is the main source of auxiliary heating on JET. With the addition of ICRH heating, D–T reactions also occur from collisions between the Maxwellian bulk ions and the fast fuel ions accelerated by RF heating, typically to $E > 100$ keV. The baseline scenario (section 3.1), operated at high $I_{\rm P}$ and plasma density, is characterized by weaker NB penetration in the plasma and higher thermal stored energy, $W_{\rm th}$, at comparable input power, therefore it maximizes the thermonuclear component on JET. In the hybrid scenario (section 3.2), the beam-target component of fusion reactions is larger, due to the lower $I_{\rm P}$ and density and thus more favourable NB penetration [37]. Exploiting these different fusion performance drives, a third scenario, the T-rich (15–85 D–T) hybrid scenario, was designed to maximize non-thermal D–T fusion power on JET with Be/W wall. Confirming the predictions based on the underlying physics, it achieved the highest sustained D–T fusion power in DTE2, establishing the new world record of 59 MJ fusion energy [38].

3.1. JET D–T baseline scenario

The JET baseline scenario is based on the full plasma current ITER scenario for the $Q = 10$ milestone. Since the installation of the Be/W wall, the baseline scenario was continually developed in D plasmas to high $I_{\rm P}$ for operation at $q_{95} \sim 3$, beta values $\beta_{\rm p} < 1$, $\beta_{\rm N} \sim 1.8$–2.0. After the initial JET-ILW phase, showing lower confinement than JET-C for plasma currents $\geqslant$2.5 MA, good confinement properties ($H_{98(y,2)} \sim 1$) were recovered for $I_{\rm P}$ up to 3.5 MA and clear progress was obtained for $I_{\rm P} = 3.6$–4 MA for the maximum heating power available on JET [12]. The JET-ILW baseline scenario recipe relied on the use of trains of small D pellets (diameter of 2 mm, length 2 mm, volume 6.3 mm^3), injected from the tokamak HFS with frequency $f_{\rm pel} \sim 30$–40 Hz, to obtain sufficiently high ELM frequencies ($f_{\rm ELM}$) to flush W (and other high-Z impurities) from the pedestal region, thus ensuring high-Z impurity and density control. With D pellet pacing the resulting ELMs are not of type I, but of high frequency/lower amplitude and compound nature. At high current, $I_{\rm P} \geqslant 3.0$ MA, the pellet ELM triggering efficiency is reduced to ∼50%–60% in baseline H-modes, but this is sufficient to ensure adequate edge W control in deuterium plasmas. The 'flat' density profile of the high current baseline scenario, with high $n_{\rm e,PED}$ and low $n_{\rm e}$ peaking, hence low normalized density gradient $R/L_{\rm n}$, results in radially outward neoclassical impurity convection and thus a hollow high-Z impurity density profile. As a consequence, a strong W impurity radiation region is localized at the plasma low field side (LFS) near the pedestal (and not in the plasma core), where it can be efficiently controlled and flushed from the confined plasma by ELMs with sufficiently high $f_{\rm ELM}$, as promoted by D pellet pacing [39]. The use of pellets also allowed for lower D_2 gas injection, compared to gas puffing only, so that steady H-mode operation could be sustained together with good pedestal and thus overall energy confinement, $H_{98(y,2)} \sim 1$ [40]. Momentum confinement is also improved with pellet pacing and lower gas fuelling (and small ELMs) [41], as a reduction of pedestal top density and concomitant increase in edge (and core) toroidal rotation is observed, for given injected NB power and torque. This is important for high Z impurity control, as modelling of W neoclassical transport in the baseline scenario [41] and hybrid scenario [42] has shown that strong rotation can reverse the W convective flux from radially inwards to radially outwards at low collisionality. From a technical point of view, relying on D pellet injection made the baseline scenario more complex to execute compared to the hybrid scenario, as simultaneous availability of maximum input power and pellet injector were required. As these optimum JET plant conditions could not always be delivered on demand and the DTE2 campaign was time bound to the end of 2021, the D–T baseline scenario experiments could not fully exploit their allocated number of pulses. Attempts to increase the plasma current from 3.5 MA to 3.8–4 MA were curtailed by the difficulty to routinely deliver sustained NBI power waveforms in excess of 30 MW, required for H-mode operation at high $I_{\rm P}$. Therefore, the plasma current for the DTE2 baseline scenario was set to 3.5 MA, with $B_{\rm T} = 3.35$ T for $q_{95} \sim 3$ and core ICRH H minority heating at 51 MHz.

Prior to DTE2, a few discharges in pure T plasmas were executed to test the impact of higher isotope mass on the scenario performance, to incorporate this knowledge in the

subsequent adaptation of the D–T plasmas without excessive use of T and neutron budgets for D–T scenario development purposes. As JET is not equipped with T pellets (as planned in ITER) and D pellets could not be injected in the pure T campaign due to 14 MeV neutron budget restrictions, the impact of higher isotope mass on the baseline scenario H-modes could only be tested in two ways: (i) tritium H-modes with gas puffing only (executed at 3.0 MA) and (ii) tritium H-modes with H-pellet pacing, which, however, introduced a significant (∼11%–14%) H concentration in the plasma, even with pellet frequency limited to 15–25 Hz. With gas puffing only, it was demonstrated, as expected, that f_{ELM} decreased significantly from D to T, leading to uncontrolled rise in density and thus radiated power, so that the pulse had to be stopped early to save on tritium consumption (as steady plasma conditions could not be recovered, letting the discharge run further would only have consumed more T without adding new scientific value). However, also with H-pellet pacing it was not possible to obtain steady T H-mode conditions [43]. It is still unclear whether this was due to insufficient ELMs flushing of high-Z impurities or different density profile peaking or a combination of both.

A 'predict first' approach for the baseline scenario with the JINTRAC [44] suite of codes coupled to the quasi-linear transport model QuaLiKiz [45] was carried out to guide the preparation of the scenario for 50–50 D–T. The modelling exercise indicated good prospects for achieving $P_{\mathrm{fus}} \sim 10$ MW under a broad range of modelling assumptions, for input heating powers ∼38 MW [46].

The best DTE2 baseline scenario H-mode (pulse #99948, 29 MW NBI + 4 MW ICRH) reached a peak fusion power of 8.3 MW, with 60% of this power from thermal fusion reactions and 40% from beam-target reactions, as calculated by TRANSP/NUBEAM, and $H_{98} \sim 0.9$ [43], see figure 1. Excellent control of the required 50–50 D–T mixture was achieved with D-pellet pacing and T gas injection, as well as with D–T NBI. However, unlike the 3.5 MA discharges in D, the scenario was not steady in D–T and could not be sustained for the target duration of 5 s. While good H-mode access was recovered after re-optimisation of this phase from D to D–T, the discharge was stopped early (to save neutrons) due to uncontrolled rise in density and high-Z impurity radiation at the LFS. Analysis is ongoing to disentangle the effect of increased density due to reduced particle transport in D–T (and T) vs D from the effect of possibly less effective ELM flushing in D–T plasmas at same pellet frequency as in D plasmas. Nonetheless, figure 2 shows that the peak fusion power achieved in DTE2 by the baseline scenario at 3.5 MA (gold stars) is in the range of the predictions based on D counterpart baseline H-modes at the same input power and (conservatively) assuming pedestal conditions invariant with isotope mass [43, 46]. Analysis and modelling are in progress to understand particle and W impurity transport in the pedestal region of the D and D–T baseline H-modes in view of extrapolation of the JET results to ITER conditions.

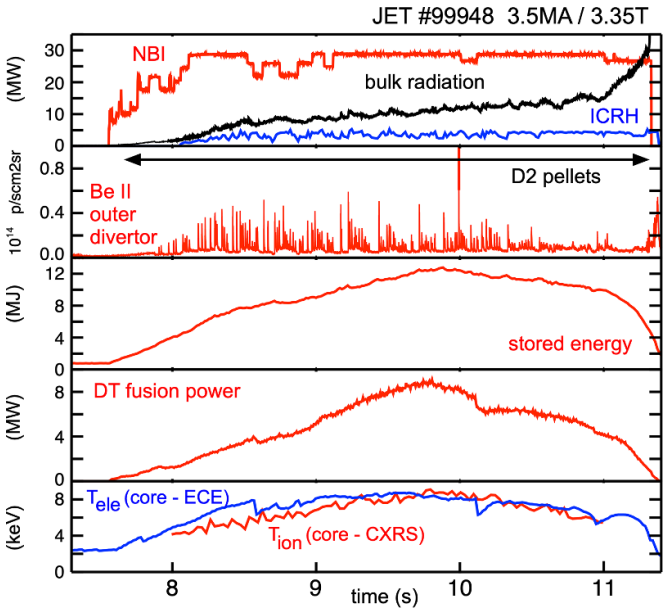

Figure 1. Best performing 50–50 D–T JET baseline scenario pulse in DTE2 (#99948, 3.5 MA/3.35 T, 30 MW NBI, 4 MW ICRH, D-pellet pacing). From top to bottom panel: (1) NBI power, bulk plasma radiation and ICRH power; (2) outer divertor Be II line intensity used as ELM marker; (3) plasma stored energy; (4) D–T fusion power; (5) core T_{e} (from ECE) at $\rho_{\mathrm{tor}} = 0.0$ and T_{i} (from CXRS) at $\rho_{\mathrm{tor}} \sim 0.2$.

3.2. JET D–T hybrid scenario

The so-called 'hybrid scenario' is an attractive operating scenario for ITER long pulse operation, aimed at maximizing neutron fluence with an extended burn time ($t > 1000$ s) for testing technologies required by a fusion power plant, and significant fusion gain $Q > 5$. It was proposed as an intermediate, or indeed 'hybrid', operating scenario with lower plasma current than the reference baseline scenario but higher than in steady state scenarios, thus saving transformer flux and allowing for longer operation in current flattop. Auxiliary current drive systems would provide a significant fraction of the plasma current, to extend the pulse duration. Thus, in the ITER hybrid scenario the plasma current is driven by a combination of inductive and non-inductive plasma currents [47, 48]. Early explorations of the operating space of the hybrid scenario, e.g. in AUG [49] and DIII-D [50], found that with reduced plasma current and modified current density profile, higher normalized pressure and energy confinement ∼20%–50% above the confinement scaling for conventional H-modes could be achieved, thus allowing for long pulse ITER operation at high fusion gain ($Q \sim 10$). An additional advantage of the ITER hybrid scenario at reduced plasma current (∼11 MA), compared to the baseline scenario (15 MA), is the reduction in risks associated with disruptions [48].

The JET D–T hybrid scenario was performed at ∼50–50 D–T isotope mixture, using D–T gas injection and

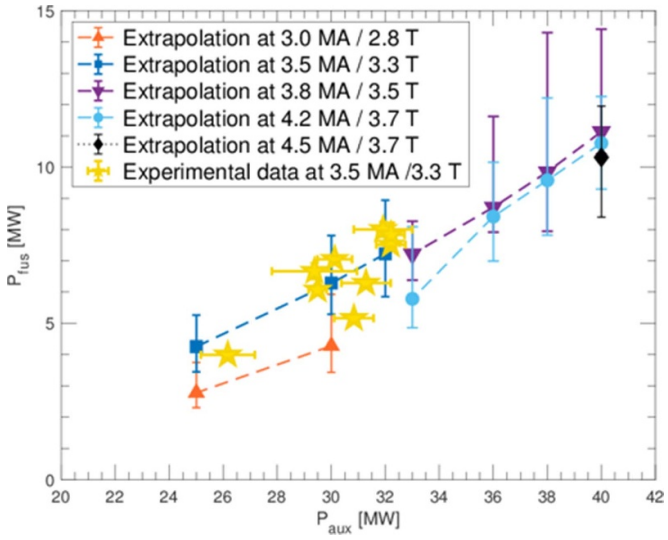

Figure 2. Comparison of D–T fusion power achieved in DTE2 by the baseline scenario at 3.5 MA (gold stars) with predictive modelling based on extrapolations from D plasmas at $\beta_N \sim 1.8$ (blue squares) using JETTO-Qualikiz within the JINTRAC workflow. The predicted D–T fusion power at 3.0 MA/2.8 T (orange up-triangles), at 3.8 MA/3.5 T (purple down-triangles), at 4.2 MA /3.7 T (cyan circles) and at 4.5 MA/3.7 T (black diamonds) are also shown. The error bars correspond to different assumptions on the thermal conductivity in the pedestal. Adapted and reproduced from [46]. © 2022 Crown copyright. Reproduced with the permission of the Controller of Her Majesty's Stationery Office. CC BY 4.0.

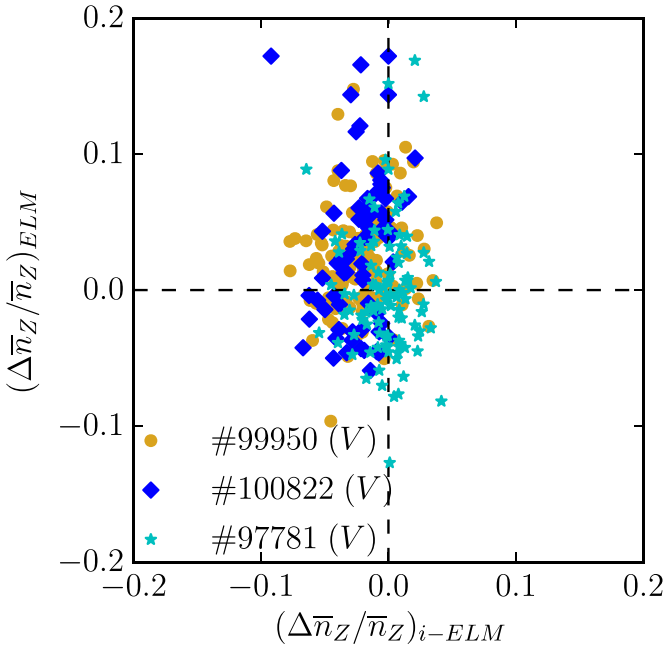

Figure 3. Change in high-Z impurity density inter-ELM (i-ELM) on x-axis and intra-ELM (ELM) on y-axis in D–T (gold) compared to D (blue and cyan). Positive numbers indicate radially inward direction of the high-Z impurity transport. With this representation, a pure screening pulse has points only in the upper left quadrant, while a purely ELM flushing pulse has points only in the bottom right quadrant. Reproduced from [51]. © EURATOM 2023. CC BY 4.0.

D–T NBI, at lower plasma current 2.3 MA/3.45 T, with H minority RF heating at 51 MHz, shaped broad q-profile with $q_0 > 1$, $q_{95} \sim 4.8$, beta values $\beta_p > 1$ and $\beta_N \sim 2.6$. It is a type I ELMy H-mode at lower density, hence deeper NBI penetration and peaked density profile, aimed at improved MHD stability and reduced core transport for improved confinement, low collisionality and $T_i > T_e$ [51]. Prior to DTE2 this scenario had never been run in D–T.

Its development on JET started at low plasma current with the C-wall, then continued in the Be/W wall environment with increase of I_P/B_T, exploiting the neutral beam power upgrade to sustain the appropriate beta values, and was successful in solving the heat load challenges on JET-ILW with ~37 MW of injected power [51]. The latter was achieved with divertor strike point sweeping [52], which was sufficient in JET to limit the surface temperature on the W-coated divertor tiles to below 1200 °C without deleterious impact on the pedestal parameters (different techniques will be needed in ITER to integrate the heat exhaust with the hybrid scenario). Optimization of the scenario in D in preparation of DTE2 demonstrated effective control of high-Z impurity edge and core radiation with the type I ELMy regime, deleterious core MHD avoidance and achievement of high neutron rates [51]. In particular, achievement of edge ion temperature gradient screening of high-Z impurities, counteracting the inward neoclassical convection of impurities (proportional to Z ∇n_e), was key to achieving steady high performance in the hybrid scenario with Be/W wall. In D, a reversal of the impurity influx inter-ELM was observed [53], such that the impurity fluxes are radially outwards inter-ELM and inwards intra-ELM, as predicted for ITER [54–56]. Figure 3 shows that crucially, owing to careful scenario development, such conditions were also achieved for the D–T hybrid plasmas, thus securing the path to steady, high D–T performance.

The choice of $I_P < 3.0$ MA was dictated by the need to test a separate path to high D–T performance from that of the high-current path tested by the baseline scenario. Increase of I_P at constant P_{in} and B_T impacts impurity behaviour, as it leads to improved pedestal MHD stability, hence decrease of f_{ELM}. This leads to reduction of W transport radially outward of the pedestal ('impurity flushing' by ELMs) not compensated by sufficient reduction of inward W convection due to the increased pedestal density, thus reduced density peaking. At maximum input power the ELM frequency can only be increased in JET either by increasing gas injection or by adding pellet pacing (the latter being the strategy adopted by the baseline scenario route). The hybrid scenario used gas injection as main actuator, therefore an optimum balance had to be found between plasma current and gas rate, to ensure high enough I_P, but low enough density for beam penetration, and low enough gas injection to prevent net loss of fusion power at high gas injection rates. The optimum plasma current was found to be 2.3 MA for the maximum heating power that could be routinely achieved within the allocated experimental time (up to 30 MW NBI+ up to 4 MW ICRH with H minority heating at 51 MHz).

The hybrid scenario development was accompanied and guided by intense 'predict-first' modelling activities and periodic validation tests with interpretive modelling of the new results obtained after each development step in D, as discussed in [14]. In addition to predictions of confinement and fusion performance for the steady state phase, state of the art multi-channel integrated modelling was also performed to predict the time evolution of the discharge, with particular emphasis on core W transport, enabling prediction of the timescale of core W accumulation and associated limitation of the scenario's high-performance phase [57]. Furthermore, predictive modelling with a QuaLiKiz neural network workflow guided the optimization of the plasma current ramp-up phase with respect to increased impurity radiation when moving from D to T plasmas [58].

Prior to DTE2, the hybrid scenario was tested in full T plasmas in the T campaign with high T-NBI to incorporate knowledge related to isotope physics and thus minimize precious neutron and T budgets for the final optimization in D–T. This entailed adjustment of the q-profile formation, re-optimization of the H-mode access phase (including time of appearance of the first ELM) and control of high-Z impurity radiation in the main heating phase, all of which are different in T vs D. In particular, the gas waveforms for the H-mode access phase had to be re-optimized to compensate for the higher density and lower ELM frequency (and thus higher radiation) in T vs D. Comparison of D and T hybrid discharges with matched input power and gas injection clearly shows that the energy confinement is higher in T [51]. Thanks to this strategy, despite the optimum operation point for high D–T performance being different from the one in D, the final optimization in D–T was achieved fairly rapidly and led to D–T fusion powers exceeding 10 MW for longer than three α-particle slowing down times, 8.3 MW averaged over 5 s and a record fusion energy of 45.8 MJ obtained with a 50–50 D–T mixture (pulse #99950, see figure 4) [51]. This pulse reached $\beta_N = 2.5$, $\beta_{pol} = 1.4$ and $H_{98(y,2)} \sim 1.2$, typical of hybrid scenario H-modes. As calculated by interpretative TRANSP simulations, the fusion power was ~60% from beam-target D–T reactions and ~40% from thermal reactions (beam–beam reactions being negligible), and ~2 MW of α-particle heating were generated in the early phase of the discharge (before decaying later in the pulse). A fusion gain of $Q_{in} = 0.32$ (defined as P_{fus}/P_{in}, with P_{in} the total input power) averaged over 1 s around peak performance and =0.25 averaged over 5 s was achieved, with $P_{in} = 33$ MW. This surpassed the previous JET record of $Q_{in} = 0.18$, steady for 5 s, obtained in DTE1 with $P_{in} = 23.8$ MW [34]. However, while the DTE1 shot with C-wall was steady (in terms of energy confinement time), with the fusion power actually increasing slightly with time due to a slight decrease of core plasma density and concomitant increase in core T_i, none of the DTE2 hybrid pulses with Be/W wall were steady over the entire 5 s duration, although high performance could be sustained. The bulk radiated power slowly increased (ultimately leading to core W accumulation at the end of the I_p flat-top phase), preceded by increased density peaking, leading to decrease of

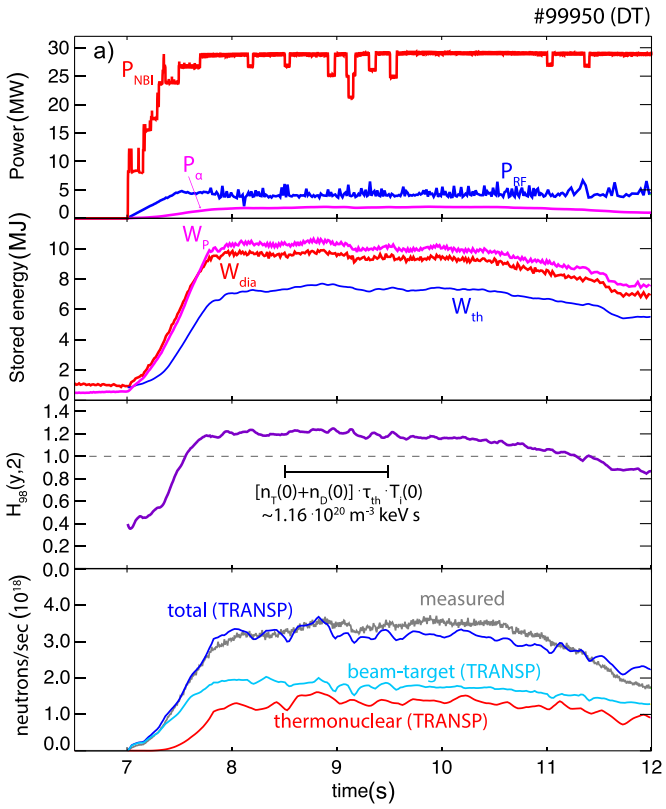

Figure 4. Time traces of main parameters of the JET DTE2 hybrid H-mode pulse #99950 (2.3 MA/3.45 T, 50–50 D–T), which set a new record fusion energy of 45.8 MJ in a 50–50 D–T mixture. Reproduced from [51]. © EURATOM 2023. CC BY 4.0.

fusion performance. In addition, a variety of NTM activity also occurred, contributing to the degradation of the plasma stored energy and of the neutron rate [51].

The maximum fusion power obtained by predictive quasi-linear modelling, using different physics workflows and modelling assumptions, is in broad agreement with the measurements in DTE2 at the given input power [14], as shown in figure 5, giving confidence in the capability of current transport models to predict fusion performance from D to D–T. However, it is important to note that not all features of reactor-relevant D–T plasmas can be fully predicted at this stage with integrated modelling. In particular, the presence of a significant population of α-particles in burning plasmas may introduce additional physics, such as core turbulence suppression by α's, a condition which could not be tested in the JET DTE2 plasmas due to the low fraction of α-particles generated, although some DTE2 experiments mimicked the impact of fast particles on D–T plasma transport [59]. Furthermore, the 'predict first activity' concentrated on core plasma predictions, either with simple scaling from D to D–T for the pedestal or neglecting its dependence on isotope mass and SOL conditions, due to lack of a fully predictive pedestal model. These are two key areas where intensive efforts should be invested.

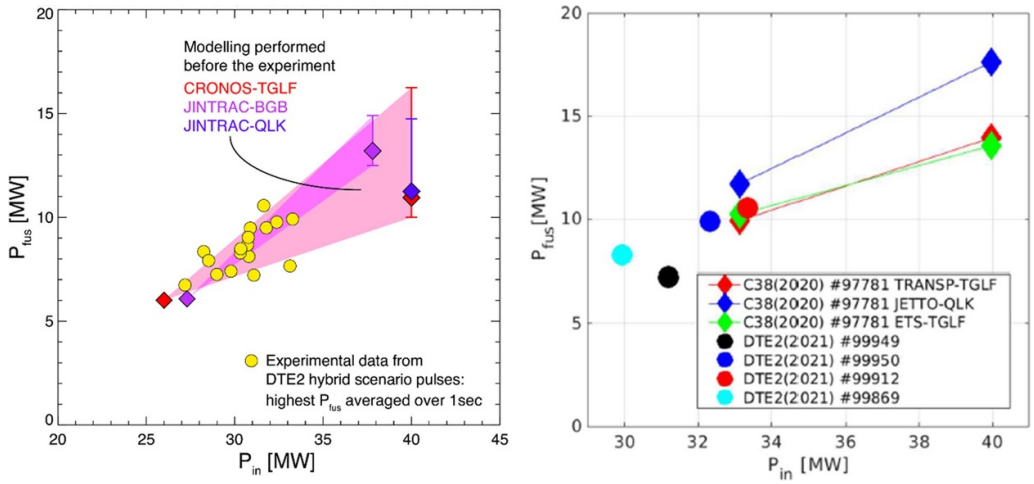

Figure 5. Comparison of predicted fusion power (diamonds) and experimental data for the DTE2 hybrid scenario (yellow circles—highest $P_{\rm fus}$ averaged over 1 s). Predictive modelling was performed with different workflows and modelling assumptions, starting from (2014 to 2018) D hybrid H-modes (Left) and from best performing, steady hybrid H-modes in (2019–2020) (Right). Reproduced from [14]. © 2023 The Author(s). Published by IOP Publishing Ltd on behalf of the IAEA. All rights reserved. CC BY 4.0.

3.3. JET T-rich hybrid scenario for optimized non-thermal fusion

The T-rich hybrid scenario was carefully optimized on JET to maximize non-thermal D–T fusion and thus obtain the highest fusion powers for the maximum available auxiliary heating, test our understanding of the underlying D–T physics and generate high 14 MeV neutron fluxes, α-heating and α-particle pressure. This careful optimization of the JET heating methods and D–T plasma mixture was guided by predictive modelling and capitalized on three key physics aspects: (i) D-NBI heating at ∼100–120 keV into T plasma; (ii) fast isotope ion transport effect allowing control of the optimal D–T mixture with the Be/W wall and (iii) D minority ICRH heating at fundamental ($N = 1$) harmonic, predicted to boost $P_{\rm fus}$ by a further ∼20% [38].

JET D–T fusion power extrapolations with TRANSP had shown that whereas with 50–50 D–T NBI injection the optimal fusion power is obtained for 50–50 D–T plasma, with D-NBI heating into a T-rich plasma (i.e. with T/(D + T) concentration maximized) up to 50% higher $P_{\rm fus}$ can be achieved than in an equivalent 50–50 D–T H-mode on JET. This is because the JET NBI heating system operates at energies of 100–120 keV, corresponding to the maximum of the D–T fusion cross section, see e.g. [36]. In the JET hybrid scenario, with relatively low density and good NBI penetration compared to the baseline scenario, high NBI heating delivers significant core particle fuelling. Indeed, a sizeable fraction of the core density peaking is due to NBI fuelling in these conditions. Conversely, gas injection predominantly fuels the plasma edge. Therefore, in the 50–50 D–T scenarios, balanced D–T NBI and D–T gas fuelling (from GIMs and TIMs) ensured 50–50 D–T mixture over the whole plasma volume. The T-rich scenario exploited instead asymmetric isotope fuelling: D-NBI provided core D fuelling and the TIMs provided T-gas injection at the plasma edge. Due to the fast isotope transport effect (fast isotope mixing), which occurs in plasmas dominated by ITG turbulence, as is the case in the core confinement region of JET, the equilibration time between isotope ions is much faster than the particle confinement time, allowing for the D–T ratio to be the same across the entire plasma radius. With strong core particle source, as in the case of the hybrid scenario, profile peaking of the total plasma density is obtained, but not of a given isotope ion. Fast isotope mixing is only observed in plasmas with multiple ion mixtures and core ITG turbulence and was first demonstrated experimentally in JET in mixed H–D H-modes at low $I_{\rm P}/B_{\rm T}$ and low NBI-heating [60] and explained by first-principle modelling [61].

ICRH can also contribute to D–T fusion via acceleration of D ions, with ($N = 1$) and ($N = 2$) D resonance heating schemes possible. However, of the two schemes ($N = 1$) is much more efficient in generating fusion power, but only if the D concentration is kept within ∼10%–30% in the plasma core, as shown previously in JET DTE1, albeit not in combination of strong NBI heating (see section 7). This RF scheme could be executed in JET DTE2 with the hybrid scenario adapted to ICRH frequency $f = 29$ MHz and operating at $B_{\rm T} = 3.86$ T, instead of 3.4 T, and at $I_{\rm P} = 2.5$ MA, instead of 2.3 MA, and was predicted to boost $P_{\rm fus}$ by an additional 20% compared to D-NBI heating only [38, 62].

In preparation of the DTE2 experiment, isotope mixture control was confirmed experimentally also at high D-NBI power (∼24 MW) and higher $I_{\rm P}/B_{\rm T}$ (2.4 MA/2.8 T) in a 'proof of principle' experiment with H–D mixture: D gas fuelling was swapped with H gas fuelling mid-pulse, demonstrating fast conversion of the plasma majority from D to H within a single high power plasma pulse [38]. These results confirmed that in JET with Be/W wall the plasma isotope composition is determined by gas injection and isotope legacy is not important (unlike in a tokamak with C-wall and thus higher fuel retention rate). Interpretative TRANSP and JINTRAC-QuaLiKiz modelling corroborated the experimental results, confirming fast isotope mixing also at high NBI power [38]. The 3.86 T/2.5 MA ($q_{95} = 4.8$) hybrid scenario was also tested

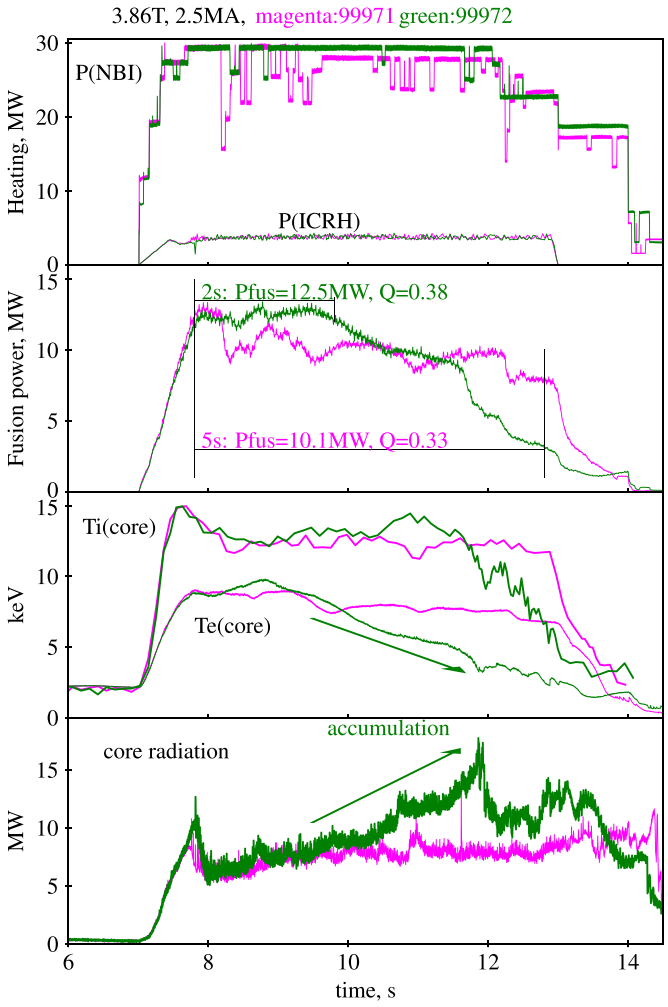

Figure 6. Comparison of the two best performing T-rich hybrid pulses at similar input engineering parameters: #99971 (magenta), with sustained high fusion power = 10.1 MW for 5 s and #99972 (green) with higher P_{fus} = 12.5 MW for 2 s, but degrading later in the discharge due to core impurity accumulation. Reproduced from [38]. © 2023 Crown copyright, UKAEA. CC BY 4.0.

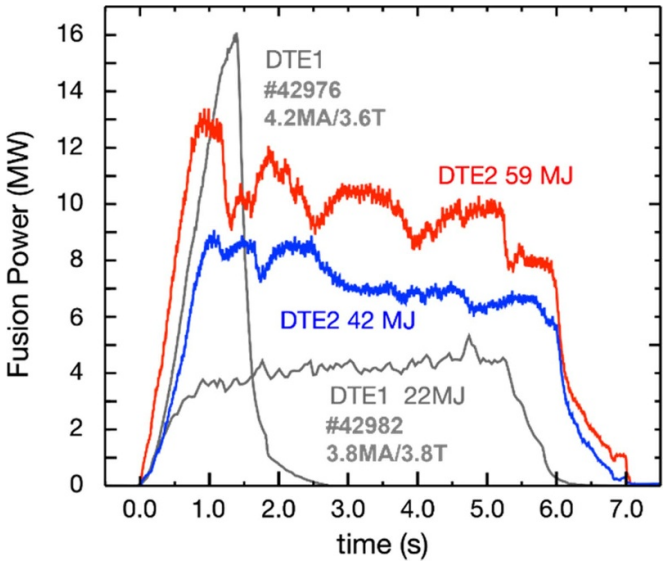

Figure 7. Comparison of world fusion energy records obtained in JET DTE1 (1997) with C-wall and in DTE2 (2021) with Be/W wall. DTE2 pulse #99869 (2.3 MA/3.45 T), blue trace, was a hybrid H-mode with 50–50 D–T generating 42 MJ of fusion energy and pulse #99971 (2.5 MA/3.86 T), red trace, a hybrid H-mode with D-NBI in T-rich plasma (15–85 D–T) to test maximum D–T performance on JET via optimized non-thermal D–T reactions and generating 59 MJ of fusion energy.

in a pure T plasma with T-NBI heating and H minority ICRH heating scheme at 54.5 MHz. Only minor modifications were then required to port the scenario from pure T plasma to the high fusion power D–T pulses.

The T-rich experiment, successfully executed in the final phase of DTE2 after conversion of the 2nd NBI box back to D, carried out 8 T-rich pulses at high D-NBI power (∼30 MW), variable T-gas dosing and ($N = 1$) D minority ICRH, fully demonstrating the underlying physics. The plasma D–T composition reached 15–85, as validated with high accuracy by neutron spectroscopy [27], similar to that of the D-H test pulses. Four pulses qualify as stable for 5 s. Seven pulses exceeded the fusion energy record of 45.8 MJ obtained with the 50–50 D–T hybrid scenario, of which pulse #99971 generated the new world fusion energy record of 59 MJ, see figures 6 and 7. We note that also the T-rich hybrid scenario, as the 50–50 D–T counterpart, is marginally stable to high-Z impurity accumulation due to its characteristic density peaking. However, unlike the 50–50 D–T hybrid scenario, which is a type I ELMy H-mode, the H-mode pedestal of the T-rich scenario was unexpectedly different: it is not type I ELMy, as evidenced by pedestal linear MHD stability analysis, and has lower pedestal density and higher f_{ELM} (∼80–100 Hz) than the 50–50 D–T hybrid H-modes counterpart (therefore displaying a different isotope mass dependence than found in type I ELMy H-modes, see section 6). Analyses are on-going to understand the physics mechanisms driving these differences. Overall, for similar values of the plasma stored energy, W_{dia}, the T-rich hybrid H-modes delivered about 50% higher fusion power than the 50–50 D–T counterpart hybrid H-modes, as shown in figure 8, in line with modelling predictions carried out in preparation of the experiments [38].

Although the T-rich scenario cannot be exploited for fusion energy production in fusion power plants, where the plasma heating must be self-sustained, it could be employed in smaller size fusion devices operated as 14 MeV neutrons source. However, more importantly, this JET DTE2 scenario acted as testbed of a variety of D–T physics aspects which were not previously tested in a tokamak. It is likely that a T-rich, high P_{fus} hybrid H-mode could not be achieved in a tokamak with C-wall, due to its large T retention, thus the JET Be/W wall was probably key to the success of this scenario in DTE2. Interpretative TRANSP modelling of JET's D–T scenarios has shown good agreement between measured and computed 14 MeV neutron rates for high performing discharges with auxiliary heating power >20 MW [37, 63]. The T-rich scenario, however, could not be fully modelled by TRANSP due to its inability to model the RF acceleration of a large

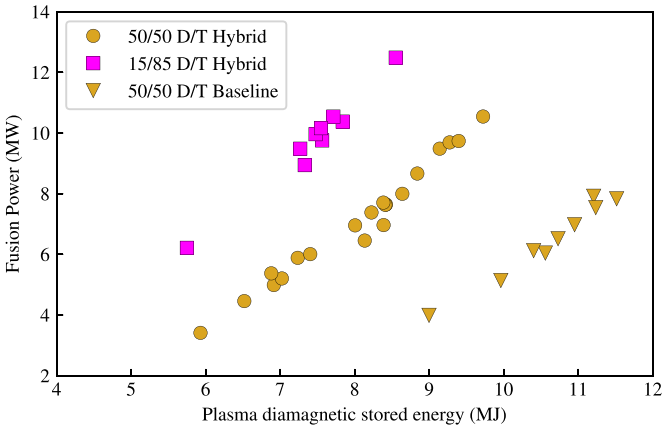

Figure 8. Measured fusion power versus plasma diamagnetic stored energy for the T-rich hybrid H-modes at 2.5 MA/3.86 T (magenta squares), 50–50 D–T hybrid H-modes at 2.3 MA/3.4 T (gold circles) and 50–50 D–T baseline H-modes at 3.5 MA/3.35 T (gold triangles). The data are averaged over the time window of [9.0–10.0]s for the hybrid pulses and over the time window [9.3–10.3]s for the baseline pulses to enable appropriate comparison (see figures 1, 4 and 6 for representative time evolution of the three scenario). Adapted and reproduced from [38]. © 2023 Crown copyright, UKAEA. CC BY 4.0.

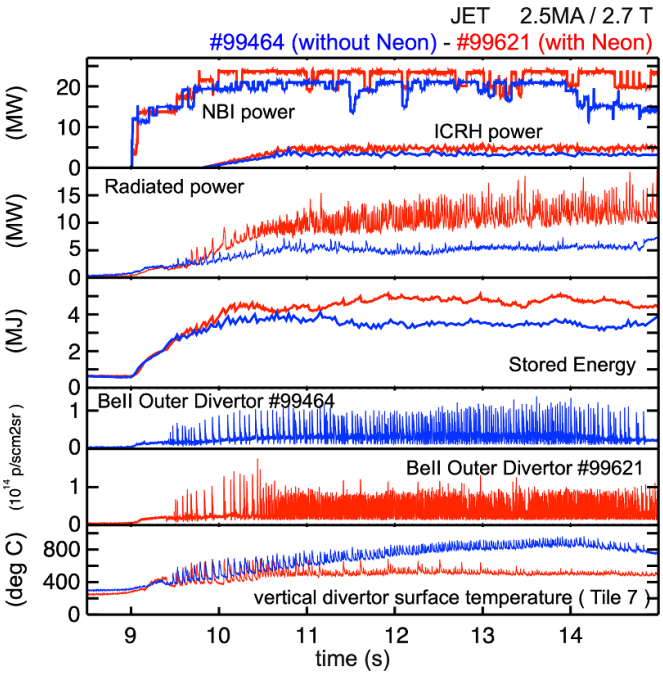

Figure 9. Integrated Ne seeded ITER baseline scenario in JET DTE2 with Be/W wall (red traces) compared to its unseeded D–T reference (blue traces). From top to bottom panels: NBI and ICRH input power; total radiated power; plasma stored energy; Be II line intensity at 572 nm from inner divertor, as ELM marker; outer divertor (vertical) target surface temperature from IR camera, showing strongly reduced divertor temperature with Ne seeding.

minority of thermal D ions. Instead, the interaction of the fast D NBI ions with RF waves can be modelled in TRANSP via a so-called RF 'kick' operator implemented in NUMBEAM [64, 65]), which communicates to NUBEAM the RF electric field components and perpendicular wave vector for each toroidal mode, as computed by the TORIC wave solver. Every time a fast ion passes through a Doppler shifted resonance layer, it receives a random 'kick' in velocity space [66], with average kick amplitude derived from quasi-linear theory [67], while the stochastic nature of the wave-particle interaction is reproduced via Monte Carlo random number for the phase of the gyro-orbit. On the other hand, NBI and ICRF power deposition and absorption profiles, including NBI + ICRF synergy, could be fully modelled for the T-rich scenario using the ETS workflow, with modelling results in agreement with experiment [38, 62], as benchmarked by neutron spectroscopy measurements, one of the many key JET upgrades for DTE2 (see section 8).

4. Demonstration of ITER-relevant, Ne-seeded radiative scenario in D–T with a Be/W wall

JET-ILW experiments in 2021 in deuterium plasmas continued to address the integration of a radiative divertor for heat load control with good plasma energy confinement. Excellent progress was made with Ne as extrinsic radiator, demonstrating a steady Ne-seeded ITER baseline scenario on JET with $H_{98(y,2)} \sim 0.9$, $\beta_N \sim 2.2$, high Greenwald density fraction $f_{GW} \sim 0.7$ and no ELMs [68]. The scenario was performed in ITER-relevant configuration at high triangularity $\delta = 0.35$, with strike points on the vertical divertor targets, at 2.5 MA/2.7 T ($q_{95} = 3.0$). The auxiliary heating was provided by NBI and RF H minority heating at 42 MHz, with best results obtained at the highest total input power of $P_{in} = 34$ MW.

The main features of the integrated Ne-seeded scenario are the reduced pedestal density and increased pedestal temperature and plasma toroidal rotation shear, leading to improved energy confinement compared to the unseeded reference plasma, as the combined effect of higher pedestal temperature, *ExB* shear stabilization and Ne impurity-induced stabilization of core ITG turbulence more than offset the increased plasma dilution at higher Z_{eff} with Ne seeding [69]. This Ne-seeded deuterium plasma was thus the reference point for porting the scenario to D–T, as a first of a kind demonstration of core-edge integration in a tokamak with metallic wall and D–T fuel (we recall that neither JET DTE1 nor TFTR D–T experiments had tested plasmas with impurity seeding).

In JET DTE2, an integrated, Ne seeded radiative H-mode was successfully demonstrated for the first time in a 50–50 D–T mixture with the ITER-like Be/W wall [68]. The steady, 5 s long, ELMy H-mode pulse achieved partially detached divertor plasma, strongly reduced divertor temperature compared to its unseeded counterpart, high radiation fraction, beta values $\beta_p < 1$ and $\beta_N \sim 1.6$, high electron density with $f_{GW} \sim 0.7$, $T_i \sim T_e$, and small/high frequency ELMs, confirming Ne as a promising extrinsic radiator for ITER. The main characteristics of the JET DTE2 Ne seeded scenario are shown in figure 9. Unlike in the JET scenarios for high fusion power at lower fuelling rates (presented in section 3), where adaptation of the scenarios from D to D–T was required to react to changes induced by the increase in isotope mass, a steady Ne seeded H-mode plasma could be ported essentially one-to-one

from D to 50–50 D–T without tuning of fuelling rates, Ne seeding rates or H-mode entry phase. The only notable exception was a limitation of the operational domain introduced by the NB re-ionisation heat load on the Be limiter in D–T (and T) [70], which ultimately limited the maximum NBI heating power to ∼23–24 MW at the high fuelling rates typical of this scenario. As a consequence, the limited NBI power unfortunately prevented reproducing in D–T a similar good performance as obtained in D at higher input power, which is required to achieve the optimum pedestal temperature needed to benefit from improved confinement with Ne as extrinsic radiator. Thus, when compared to the IPB98(y,2) scaling [71], the thermal energy confinement time of the DTE2 Ne-seeded plasma shown in figure 9 was modest, with H98(y,2) ∼ 0.65 (we note that the H98 factor is quoted here simply to give an estimate of how the achieved plasma stored energy, for the given amount of heating power, compares to the standard H-mode scaling, as it is well known that the IPB98 scaling was not derived from plasmas at high radiated fractions). Due to the above mentioned NBI technical limitations and the lack of further experimental time in the DTE2 campaign, the D–T Ne seeded scenario could not be optimized in 2021 (this optimization was carried out in 2023 and will be reported in separate publications). Nonetheless, the main scenario features, namely the integration of partial detachment, strongly reduced divertor heat loads and small/high frequency ELMs with Ne seeding in a 5 s long, steady discharge were similarly achieved in D–T as in D, providing very encouraging results for ITER [68].

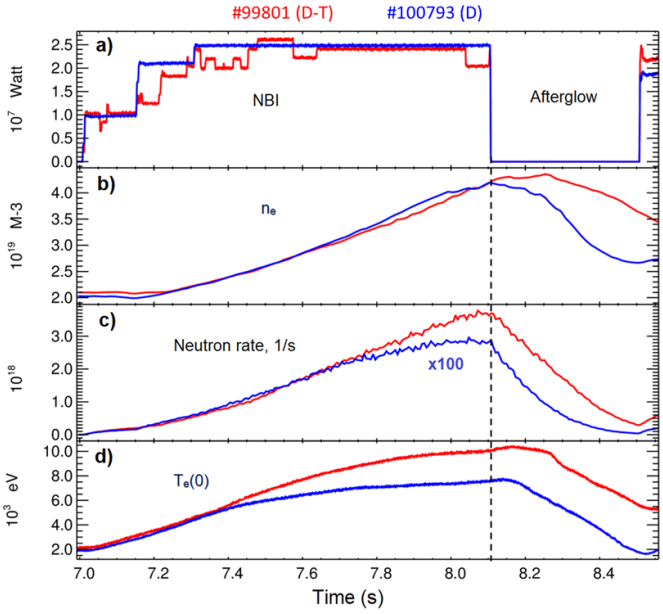

Figure 10. Time traces of JET D–T pulse #99801 (red) vs its D reference counterpart pulse #100793 (blue) at 2.3 MA/3.45 T: (*a*) NBI heating power, with afterglow phase starting at $t = 8.1$ s (marked by vertical dashed line); (*b*) central line averaged density; (*c*) neutron rate and (*d*) core electron temperature by ECE. Reproduced from [73]. CC BY 4.0.

5. Demonstration of clear α-particle effects

The fusion products of D–T reactions, α-particles, are born with an average energy of 3.5 MeV and transfer their energy to the thermal plasma (mainly electrons) during their slowing down phase, thus providing the self-heating of a sustained D–T burning plasma. Confinement of α-particles is therefore key to the efficient heating of the bulk plasma of a D–T reactor. Due to their high energy, α-particles are also expected to be resonant with Alfvén waves. Redistribution of fast ions can lead to enhanced fast ion transport and thus degrade fusion performance in a reactor and also potentially damage its plasma-facing components if a sizeable amount of energetic particles are redistributed onto unconfined orbits during their interaction with Alfvén waves. Therefore, obtaining measurements of α-heating and α-particle driven effects in current D–T experiments is crucial. Indeed, JET was designed from the start with one of the main objectives being the study of α-particle production, confinement and consequent plasma heating. Although α-particle effects were observed in TFTR D–T experiments (1994–96) [6], JET DTE1 results on α-particles were somewhat ambiguous [72]. For this reason, in DTE2 emphasis was placed on designing experiments which minimized effects due to other fast ion populations and enabled unambiguous observation of α-particle signatures in high fusion power D–T plasmas.

A rich set of unique observations on α-particles were obtained in DTE2 in reactor relevant conditions [59], enabled by the new fusion diagnostics installed on JET since DTE1 [27]. In particular, neutron and γ-ray spectrometers, a 2D neutron/γ-ray camera for tomographic reconstruction of the α-particle source and temporal evolution of its spatial profile, a FILD with energy and pitch-angle resolution and a set of lost α-particle collectors (Faraday Cups) with poloidal, radial and energy resolution. In fact, a much richer variety of observations of α-particle driven instabilities was collected in DTE2 than anticipated when designing the experiments, highlighting the vital need for α-particle studies for understanding and prediction of burning plasmas.

5.1. α-particle heating

Direct evidence of electron heating of D–T plasmas by α-particles was obtained in the NBI after-glow phase of transient high-performance scenarios with ITB, reaching maximum $P_{\rm fus} \sim 12$ MW [73]. The core electron temperature was ∼30% higher in D–T than in the reference D plasma and in the after-glow phase, namely the discharge phase with NBI switched off, while the 14 MeV neutron rate kept decreasing, the core electron temperature increased and then remained constant at ∼10 keV for ∼130 ms after NBI switch-off. This is direct evidence that in the afterglow phase the 3.5 MeV α-particles continued to transfer their kinetic energy to the plasma electrons during the α slowing down time, since the D and T NBI ions mostly heat the plasma bulk ions. Conversely, in the reference D plasma, both core $T_{\rm e}$ and D neutron rate decreased in the after-glow phase (see figure 10). Interpretive transport

modelling with TRANSP of the D–T plasma and its D reference confirms the observation of α-heating. The thermal component of the neutron rate dominates during both the high-performance phase and the after-glow phase of the D–T discharge. Conversely, in the D reference plasma the beam-target component dominates throughout the entire NBI phase and in the afterglow phase the neutron rate decays two times faster than in the D–T plasma counterpart. In D–T, the α-particle power to electrons increases during the NBI heating phase and continues to rise for ∼200 ms in the afterglow phase, up to ∼1.5 MW [73].

Heating of bulk electrons by fusion born α-particles was also detected exploiting the dynamic response of T_e to ICRH power modulation using the fundamental D RF heating scheme in a T-rich hybrid H-mode with D-NBI (described in section 3.3). The modulation of T_i and of the fast D ions (both D bulk ions and D-NBI ions) accelerated by ICRH leads to modulation of α-heating, which in turn yields a significant phase delay (∼40°) between the measured central T_e and T_i inside $\rho_{tor} \sim 0.3$. The latter can only be explained by α-particle heating and quantitative agreement with experiment is obtained with the ETS/HCD workflow [74].

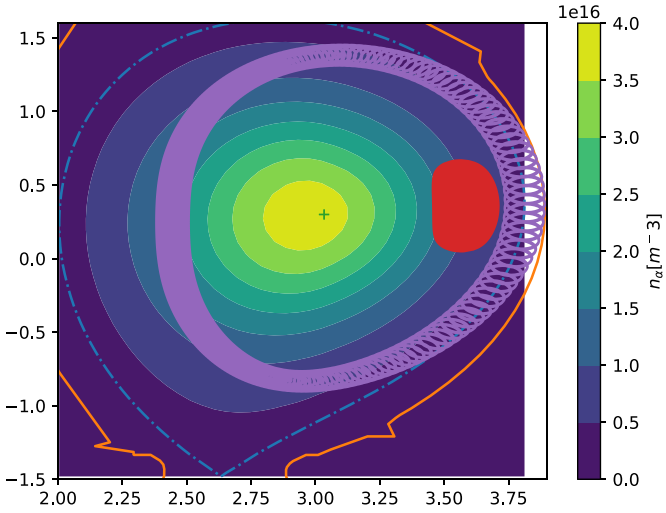

Figure 11. Contour plot of α-particle density from TRANSP with superimposed two typical 3 MeV orbits from trapped (red) and passing (purple) resonances calculated by the HALO code. Reproduced from [76]. © 2023 Crown copyright, UKAEA. CC BY 4.0.

5.2. Observation of α-driven toroidal Alfvén eigenmodes (TAEs)

TAEs are instabilities driven through resonant wave-particle interactions with α-particles. As it is difficult to obtain a sufficiently large α-particle population in JET to drive TAEs, in order to maximize the chances of such effects to be observed in DTE2, a scenario with transient ITB at 3.4 T/2.5 MA with elevated safety factor $q_0 > 1.5$, NBI heating only and with so-called 'afterglow' was developed in JET-ILW deuterium plasmas [75], to be exploited in DTE2 experiments. No ICRH was used in this scenario, to ensure that the only fast ion populations exceeding the Alfvén velocity were those produced in the fusion reactions. A TAE driven by α-particles, with α-particle drive and thermal damping modelling consistent with the observed unstable mode, was observed in JET D–T pulse #99946 with ITB during the afterglow phase, ∼50 ms after NBI switch-off [76]. The TAE mode, detected with magnetics, reflectometry, interferometry and soft x-ray emission, was located far from the core plasma, at the outer midplane, and identified as being $n = 3$ or $n = 4$. Modelling indicates it to be driven by both trapped and passing α-particles, despite the α-particles originating in the plasma centre (see figures 11 and 12). The detection of this weak mode at the plasma edge of JET, despite the weak α-particle drive, was possible because both NBI and radiative damping of the mode were also small. A linear ideal stability analysis workflow with high accuracy was required to interpret the JET measurements and accurately predict the stability of the TAE with linear drive $\gamma/\omega \sim 0.3\%$, a challenging task, thus validating modelling tools for ITER, for which stronger γ/ω drives of order 5% are expected [76].

5.3. Excitation of Alfvén eigenmodes by α-particles with bump-on-tail distribution

The excitation of Alfvén eigenmodes by a 'bump-on-tail' (BOT) α-particle distribution was also demonstrated in DTE2 [77]. To achieve this goal, experiments were carried out with NBI-only heating (2.5 MA/3.7 T, NBI 10–15 MW, no ICRH) to ensure that fusion-born α-particles would be the only ions at MeV energies present in the JET D–T plasmas. The NBI power was modulated on a time scale shorter than the α-particle slowing down time, to enable modulation of the α-particle source (given that the dominant component of the D–T fusion power was from beam-target reactions) and thus sustainment of a BOT α-particle distribution. The relative depth of the NBI power modulation, rather than its absolute value, was important for achieving a BOT in α-particle distribution. In the D–T experiments, high frequency modes were detected in the TAE frequency range with interferometry, soft x-ray and reflectometry diagnostics, and were localized close to the magnetic axis. Measurements of fusion-born α-particles were obtained with the FILD and Faraday cups. α-particle distributions with BOT in energy were indeed achieved in certain time intervals in these D–T plasmas, as confirmed by post-discharge analyses with the Fokker–Planck predictive code FIDIT [78] employed before the experiment for designing the experimental scenario, as well as with the more complete interpretative TRANSP code. However, no clear correlation could be drawn between the phases with excitation of the high-frequency modes and the time intervals with BOT. MHD and kinetic modelling indicate that a core-localized TAE with $n = 9$ is the likely mode to have been excited in the TAE frequency range and was driven primarily by on-axis beam ions.

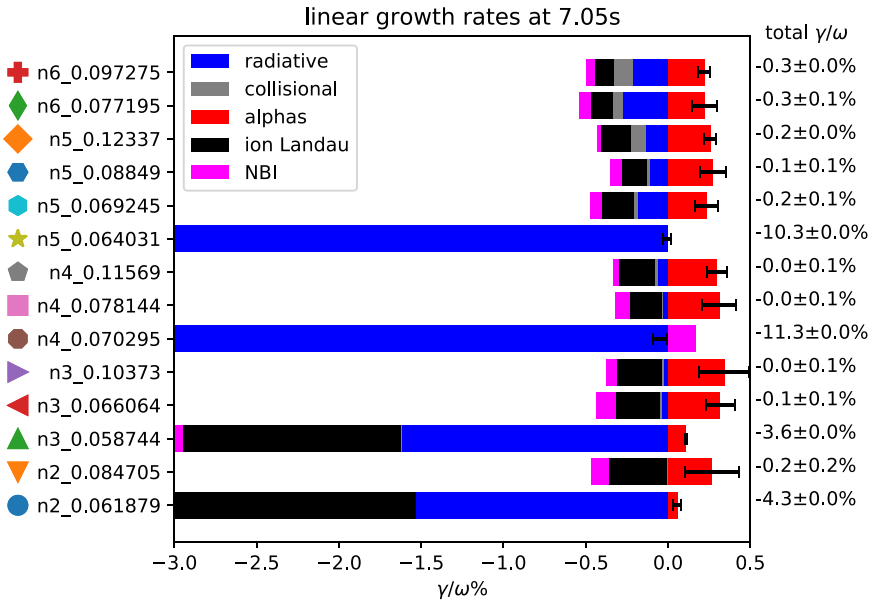

Figure 12. Contributions by drive and damping to linear growth rates γ/ω of various TAE modes calculated by MISHKA from JET D–T pulse #99946, indicating α-driven TAE observation for a mode with $n = 3$ or $n = 4$. Reproduced from [76]. © 2023 Crown copyright, UKAEA. CC BY 4.0.

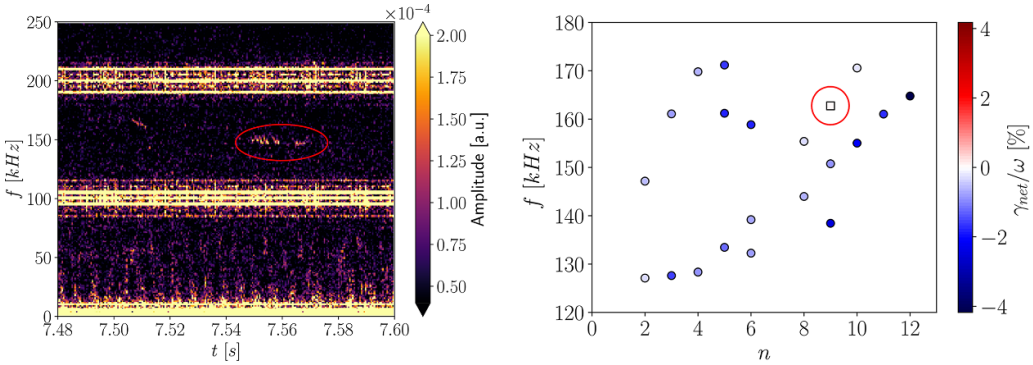

Figure 13. (Left): spectrograph of density perturbations measured by the fast far-infrared interferometer in JET D–T pulse #99503. The modes of interest (identified as a-driven TAEs—see right panel) are observed at $f = 156$ kHz at $t = 7.55$ s. (Right): calculated net growth rates γ normalized to the wave frequency ω for 21 TAEs with toroidal mode numbers n and lab frame frequencies f. The single net-driven TAE mode, $n = 9$, with lab frequency $f = 163$ kHz and core localized, is marked with a square (net damped modes are marked with circles). Reproduced from [79]. © 2023 Crown copyright, UKAEA. CC BY 4.0.

The smaller drive by α-particles pressure gradient is responsible for the mode excitation, having provided sufficient, albeit weak, drive to overcome marginal stability [79] (see figure 13). A key aspect of the analysis was the use of full orbit calculations for both NBI and α-particles, as guiding centre calculations were found to significantly overestimate growth rates. Short-lived modes were also observed in a wider frequency range up to 450 kHz in these D–T plasmas and have been identified as on-axis kinetic Alfvén eigenmodes, which were predicted in the 1970s by [80]. These modes are likely to have been driven by a BOT α-particle distribution, rather than the radial gradient of the distribution function, and investigation of their stability is the subject of follow-up studies.

5.4. *α-particle losses*

A variety of low frequency MHD modes were observed before and during the after-glow phase in high performance D–T discharges with only NBI heating and α-particle losses associated to these MHD modes were observed with the FILD and Faraday cups diagnostics. In particular, a large expulsion of 3.5 MeV α-particles, originating from the plasma core and causing a decrease in core T_e, was observed in the after-glow phase [81]. Numerical modelling is on-going to interpret these observations. In the baseline and hybrid D–T scenarios α-particle losses were found to be correlated with fishbones activity [81]. High energy α-particle loss

spikes, correlated to ELMs, were also observed and calculations of their orbits indicates that they are related to α-particles lost at the boundary between passing and trapped particles. A striking difference in the structure of α-particle losses was detected by the FILD in plasmas heated by the novel 3-ion (T-^{9}Be-D) ICRF heating scheme (see section 8): while the losses are core-localized in plasmas at $I_P = 2$ MA, they exhibit a pattern with two maxima at different pitch angles at $I_P = 2.5$ MA, the physics reason of which is under investigation.

5.5. Novel fusion γ-ray measurements

New fusion γ-ray measurements were obtained for the first time in a magnetically confined fusion plasma: 17 MeV γ-rays from T (D,γ) ^{5}He* reactions were measured in DTE2. This γ-ray emission offers the potential to be used as an additional/alternative tool to the 14 MeV neutron rate for D–T fusion power monitoring in a reactor [27, 81]. The difficulty of this method stems from the very weak and not well known γ/n branching ratio ($\sim 10^{-5}$–10^{-6}) and the need for absolute calibration of the γ-ray detector. However, for DTE2 JET was equipped with a set of fission chambers calibrated with high precision and the carefully designed tangential γ-ray detector [82], so that the combined analysis of both neutron and γ-ray emission measurements could determine the γ/n branching ratio for tokamak D–T plasma conditions [81]. The γ-ray spectra obtained in DTE2 are also helping to refine the current conceptual design of the radial γ-ray spectrometers for ITER [27].

6. Clarify isotope effects on energy and particle transport and explore consequences of mixed species plasma

6.1. Isotope dependence of L–H power threshold and L–H transition physics

First ever measurements of the L–H power threshold ($P_{L–H}$) in pure tritium and in D–T and H–T mixtures in a tokamak with Be/W wall were obtained [83, 84], providing a wealth of new information to validate L-mode transport and L–H transition models. At a given line averaged density in the high-density branch of $P_{L–H}$, the L–H transition occurs at lower edge power flux with increasing isotope mass, but for very similar n_e and T_e profiles (within experimental uncertainties) regardless of effective isotope mass A_{eff} or isotope composition [84]. A_{eff} is defined as: $A_{eff} = (c_H + 2\ c_D + 3c_T)/(c_H + c_D + c_T)$, with $c_i = n_i/n_e$, for i = H, D, T. Furthermore, P_{sep} at the L–H transition ($P_{sep} = P_{loss} - P_{rad,bulk}$, with P_{loss} the loss power and $P_{rad,bulk}$ the power radiated in the bulk plasma), normalized to the ITPA L–H scaling [85], does not scale in a simple fashion with A_{eff}. Instead, it is different in plasmas with the same A_{eff} but different isotope composition, at otherwise constant parameters (see figure 14): for instance, at a given density, it is lower for a pure D plasma than for a 50–50

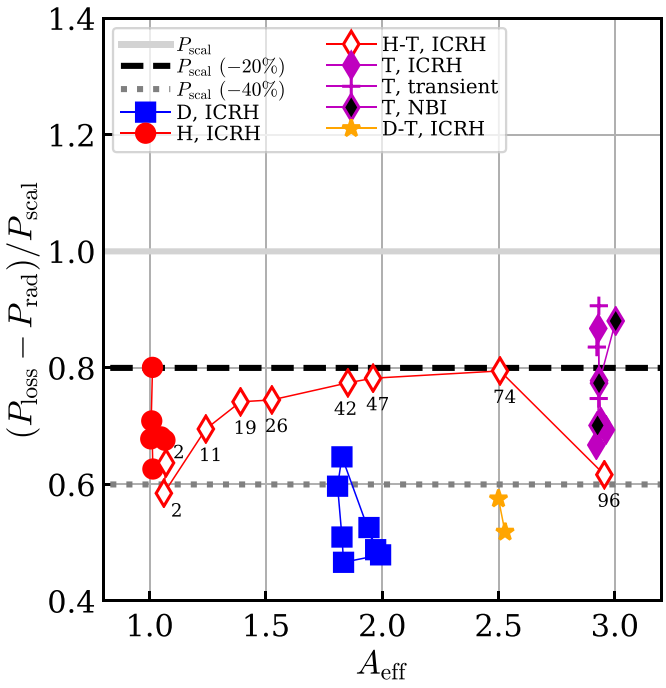

Figure 14. P_{sep} normalized to the ITPA scaling [85] for D plasmas vs A_{eff} for the L–H dataset at 1.7 MA/1.8 T (high density branch only). Reproduced from [84]. © The Author(s). Published by IOP Publishing Ltd CC BY 4.0.

T–H mixture, despite both plasmas having the same $A_{eff} = 2$. Furthermore, an offset linear relation is found between P_{sep} and the effective heat transport in L-mode prior to the L–H transition (see figure 15). These observations strongly suggest that the edge L-mode transport determines the power (P_{sep}) required to reach the critical profiles for the L–H transition, as previously reported for H and D plasmas [86], and that the isotope dependencies of P_{sep} are in fact '*inherited*' from the isotope dependencies of the edge L-mode transport before the L–H transition. It was also observed that the value of the line averaged density at which $P_{L–H}$ is minimum in JET-ILW, $n_{e,min}$, decreases with isotope mass from to D to D–T to T [83], consistent with earlier $P_{L–H}$ results in H and D plasmas [86]. These observations suggest that it may be easier in ITER D–T phases to access H-mode in T-rich plasmas [83]. Regarding figure 14, we recall that the L–H transition power threshold in JET-ILW is lower than the ITPA scaling [85] by 10%–50% due to the 'metallic wall effect' found in JET with Be/W wall [87] and AUG with W wall [88]. Furthermore, as discussed in reference [83], the ITPA $P_{L–H}$ scaling does not fit well the JET-ILW L–H data.

6.2. Isotope dependence of H-mode pedestal and core transport

Different experiments were executed in type I ELMy H-modes to disentangle the impact of isotope mass from that of other interlinked physics parameters on heat and particle transport, as it is essentially impossible to only vary the isotope mass in

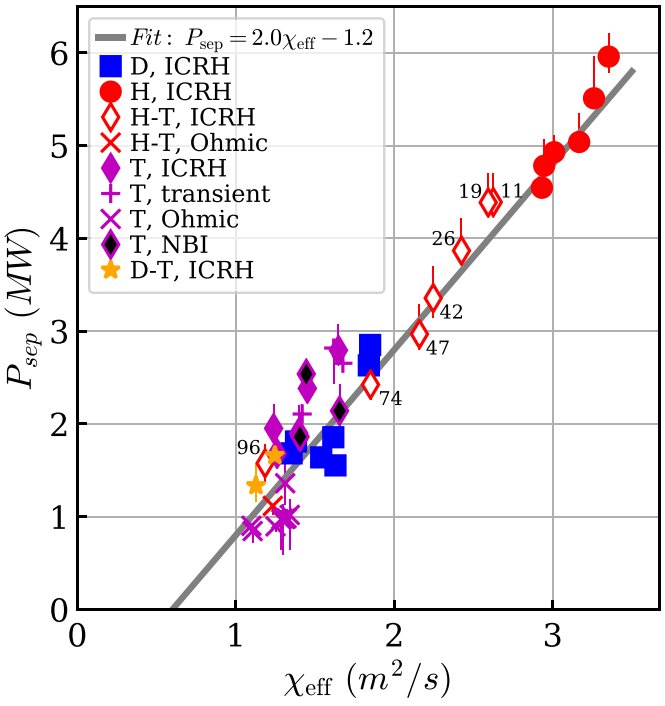

Figure 15. P_{sep} vs effective, one fluid heat diffusivity. Reproduced from [84]. © The Author(s). Published by IOP Publishing Ltd CC BY 4.0.

experiment. In all such experiments, though, a strong increase in pedestal particle confinement with A_{eff} was observed, confirming earlier studies in H and D [86, 89, 90].

In one experiment in which key parameters known to affect the pedestal behaviour were kept constant within technical capabilities (normalized total plasma pressure β_N, ratio of separatrix to pedestal density $n_{e,sep}/n_{e,PED}$, pedestal ion Larmor radius and toroidal rotation), A_{eff} was varied from D to T at constant injected gas rate in type I ELMy H-modes [91]. To ensure plasmas at similar $\beta_N \sim 1.5$ as A_{eff} was varied, the input NBI was operated in feedback control, resulting in higher P_{NBI} in D than in T due to the increase in energy confinement with isotope mass. In turn this led to a variation in ELM frequency (f_{ELM}) with heating power and A_{eff} coupled together, though it is shown that in large part f_{ELM} increased with power. In the experiment, an increase in pedestal pressure was observed from D to T, primarily driven by a large increase in pedestal density, due to steepening of the density gradient, as shown in figure 16, while $T_{e,PED}$ weakly decreased with A_{eff} ($T_{i,PED} \sim T_{e,PED}$). The experimental observations indicate a reduction in inter-ELM particle transport with increasing A_{eff}, supported by initial, linear gyrokinetic modelling of the D and T H-mode pedestals, and in qualitative agreement with recent global non-linear gyro-kinetic simulations of JET-ILW H and D type I ELMy H-mode pedestals [92]. It is to note, however, that a difference in the particle source when A_{eff} is increased from D to T (which could not be quantified in the experiment) cannot be excluded. Whereas the pedestal collisionality, ν^*_{ped}, increased by a factor of two from the D to the T plasma, based on previous scaling [93, 94] such a variation is not expected to have impacted on the results of this experiment, as discussed in [91].

In the D–T scan, improved pedestal stability with increasing A_{eff} is found when resistive (rather than ideal) linear MHD is used to model peeling-ballooning modes for the ELM onset [91, 95], in qualitative agreement with the observations. The experimental and modelling results indicate that both a reduction in inter-ELM pedestal particle transport and an improvement in pedestal stability from D to T (see figure 17) are required to interpret the pedestal changes with A_{eff}. We note again that these JET T and D–T experiments were carried out in type I ELMy H-mode, however ITER, DEMO and other fusion reactors will need to operate at high pedestal pressures but without large type I ELMs to ensure the divertor components lifetime. Therefore, understanding—both via experiments and via theory and modelling—and predictive capability of the isotope dependence of pedestals without ELMs or with acceptably small ELMs is required.

In a different set of experiments in H, D, T and ~50–50 D–T, with gas scans at fixed input power, $I_P/B_T = 1.4$ MA/1.7 T and β_N varying from 1.0 to 3.0, a different isotope mass scaling is observed for the pedestal density depending on the gas fuelling rate: in tritium $n_{e,PED}$ increases without degrading the pedestal pressure, in contrast to D and H plasmas (see figure 18) [96]. The pedestal energy confinement time $\tau_{E,th,PED} = W_{th,PED}/P_{sep}$ is found to decrease with ELM frequency, f_{ELM}, independent of isotope mass, although the lowest values of $\tau_{E,th,PED}$ and highest f_{ELM} are found for H pedestals. Indeed, the ELM characteristics are different in H, D, T, in particular f_{ELM} (T) < f_{ELM} (D) < f_{ELM} (H) for pulses with the same engineering parameters, consistent with earlier findings in H and D [86]. The plasma core thermal energy confinement time $\tau_{th,core}$ (with $\tau_{th,core} = W_{th,core}/P_{sep}$ and $W_{th,core} = W_{th}$–$W_{th,PED}$) increases with pedestal pressure for all isotope masses due to kinetic profile stiffness (and due to electromagnetic turbulence stabilization at higher β_N values). It is interesting to note that when T_{PED} and $n_{e,PED}$ can be matched by varying gas rate and plasma shaping at constant heating power of 10 MW, $\tau_{th,core}$ is similar with all isotope masses (see e.g. at $W_{th,PED} \sim 0.8$–0.9 in figure 19). At higher pedestal stored energies, typically obtained at higher heating powers, T and D–T plasmas have higher $\tau_{th,core}$ than H and D even with matched pedestal stored energies (see figure 19). For tritium, this $\tau_{th,core}$ improvement is primarily due to the unique combination of higher $n_{e,PED}$ and moderately lower $T_{e,PED}$ than in H and D and higher $\nabla T/T$ to transport the same amount of heat [96]. These measurements are broadly reproduced by quasi-linear flux driven simulations using ASTRA-TGLF (SAT2), which exhibit only a weak negative mass dependence on core transport ($W_{th,core} \sim A^{-0.16}$), with the pedestal experimental values (which strongly depend on A_{eff}) set as boundary condition. However, the quasi-linear modelling overestimates the core heat and particle transport with increasing β_N for all isotopes. A strong correlation is also found for the ratio of modelled to measured core stored energies, $W_{th,core}$ (TGLF)/$W_{th,core}$ (EXP), vs the total heat flux normalized to

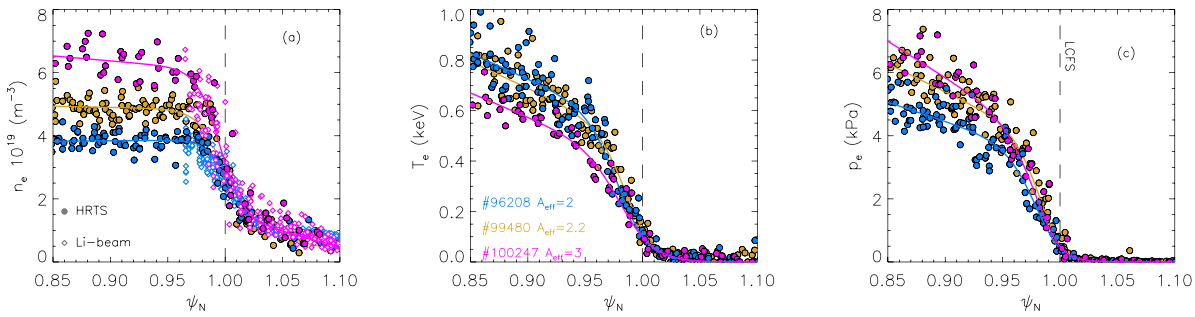

Figure 16. Pre-ELM profiles of electron density (*a*), temperature (*b*) and pressure (*c*) of the D–T scan at constant β_N and gas rate: D (#96208, blue), D–T (#99480, gold) and T (#100247, magenta) from HRTS (circles) and Li-beam (diamonds). Reproduced from [91]. © 2023 The Author(s). Published by IOP Publishing Ltd on behalf of the IAEA. All rights reserved. CC BY 4.0.

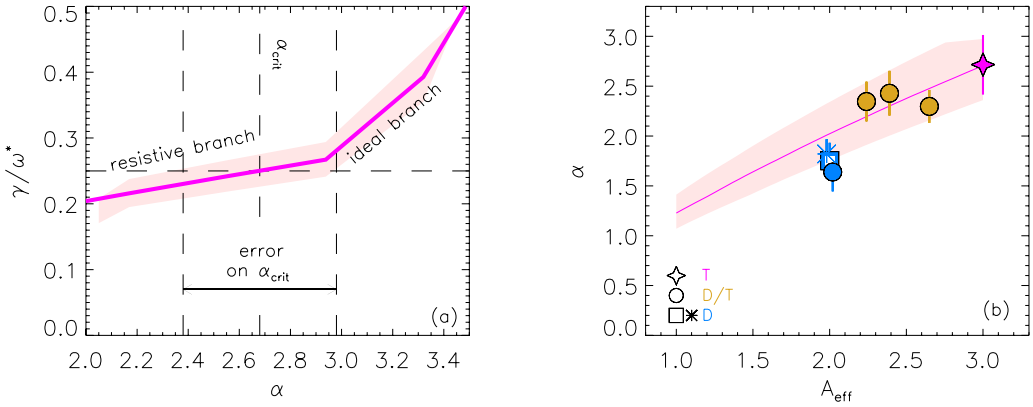

Figure 17. (*a*) Growth rate of the most unstable mode, relative to diamagnetic frequency ω^*, versus maximum normalized pressure gradient α, from resistive linear MHD stability. The calculation is for the experimental value of pedestal current density j of the T pulse of the D–T scan; (*b*) variation of α vs $A_{\rm eff}$: experiment (symbols) vs critical α (solid line). Reproduced from [91]. © 2023 The Author(s). Published by IOP Publishing Ltd on behalf of the IAEA. All rights reserved. CC BY 4.0.

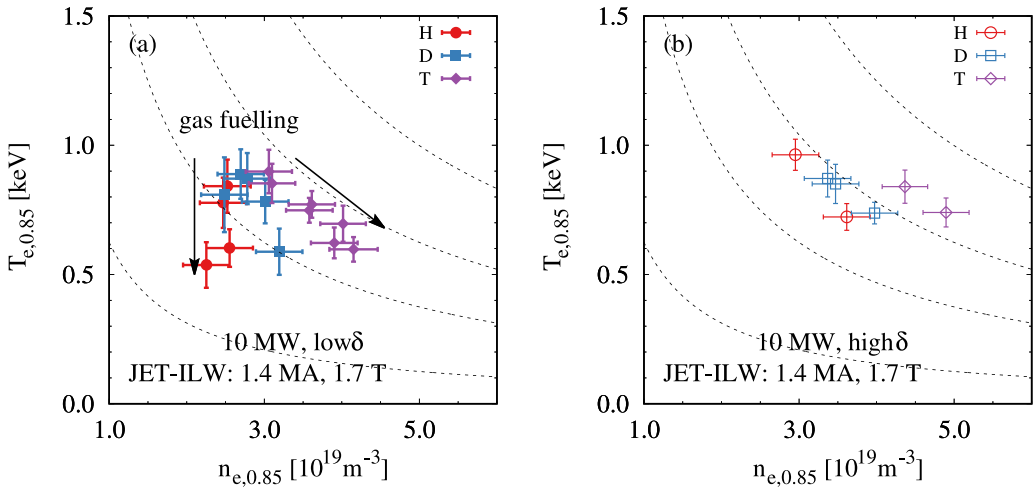

Figure 18. Edge T_e vs edge n_e (at $\rho_{\rm tor} = 0.85$) for H, D, T type I JET-ILW ELMy H-modes at same I_P/B_T and $P_{\rm NBI} = 10$ MW with different gas fuelling rates: discharges at low $\delta \sim 0.22$ (*a*) and higher $\delta \sim 0.33$ (*b*). Dashed lines are the isobars at $p_{\rm PED} = 1, 2, 5, 8$ kPa. Reproduced from [96]. © 2023 The Author(s). Published by IOP Publishing Ltd on behalf of the IAEA. All rights reserved. CC BY 4.0.

heat flux in gyro-Bohm units, $Q_{\rm tot}/Q_{\rm gB}$ at $\rho_{\rm tor} = 0.5$. Indeed, it is shown that ASTRA-TGLF (SAT2) overestimates the transport for increasing β_N or decreasing $Q_{\rm tot}/Q_{\rm gB}$, resulting in underprediction of the core stored energy. Since low $Q_{\rm tot}/Q_{\rm gB}$ values correspond to conditions close to turbulent threshold, a few pulses in tritium at $\beta_N \sim 1$ and low $Q_{\rm tot}$ (albeit closer to $P_{\rm L–H}$ than the rest of the dataset and not in the type I ELMy regime) were added for comparison (see figure 20), as they break the correlation of high β_N and low $Q_{\rm tot}/Q_{\rm gB}$ in the dataset. As can be seen in figure 20, ASTRA-TGLF (SAT2)

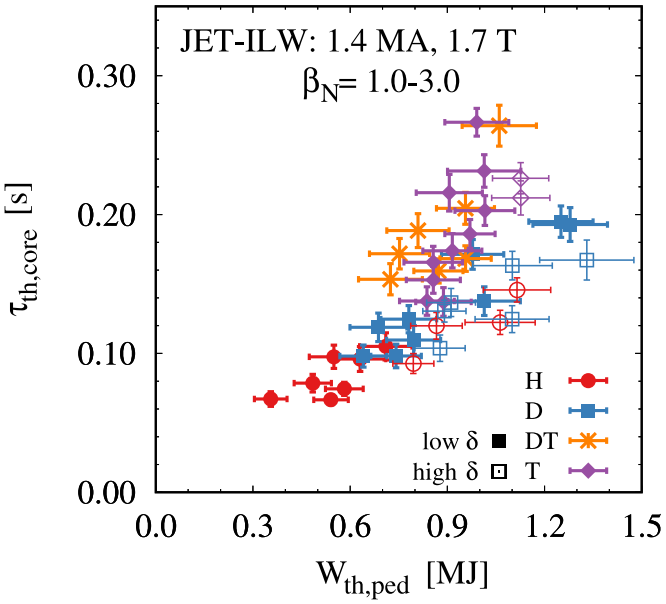

Figure 19. Core thermal energy confinement time vs pedestal thermal stored energy for the H, D, T, D–T dataset at 1.4 MA/1.7 T. Reproduced from [96]. © 2023 The Author(s). Published by IOP Publishing Ltd on behalf of the IAEA. All rights reserved. CC BY 4.0.

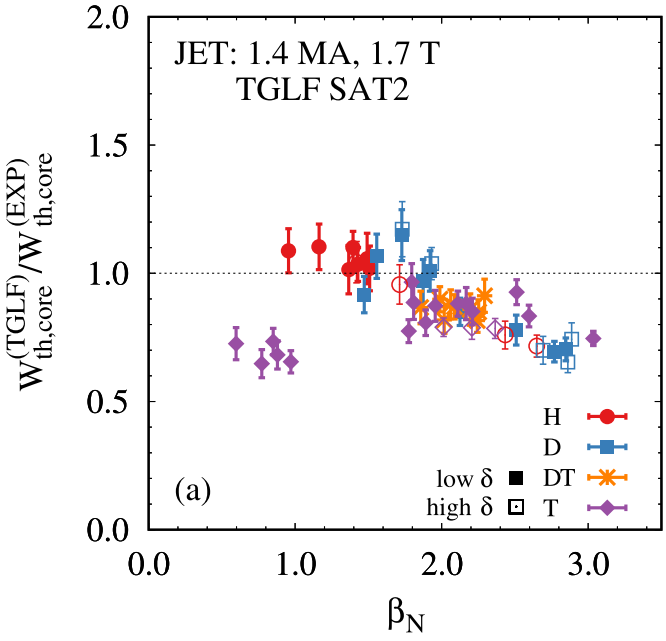

Figure 20. Comparison of ASTRA-TGLF (SAT2) predictions of core thermal stored energy $W_{th,core}$ and experimental value $W_{th,core}$ (EXP) = W_{th}–$W_{th,PED}$ vs β_N showing increasing underprediction by ASTRA-TGLF with increasing β_N. Tritium data at $\beta_N \sim 1$ are shown for comparison (although not in type I ELMy regime). Reproduced from [96]. © 2023 The Author(s). Published by IOP Publishing Ltd on behalf of the IAEA. All rights reserved. CC BY 4.0.

overestimates the transport also for these plasmas. The underprediction of $W_{th,core}$ is due to underprediction of all channels, n_e, T_e and T_i, with similar magnitude. In view of applicability of current quasi-linear modelling to predict the performance of future fusion devices, this JET-ILW dataset represents a very valuable and unique test bed for modelling validation and efforts are required to pinpoint the physics in TGLF at the origin of its discrepancy with experiment in the regime of low gyro-Bohm heat fluxes. While future fusion reactors will be predominantly heated by α-particles, non-linear stabilization of core turbulence by α-particles is not yet implemented in the QL models, nor this effect could be tested against this particular JET dataset due to the negligible α-particle population in these plasmas.

6.3. Divertor target power loads in T vs D type I ELMy H-modes

First measurements of divertor target power loads in tritium were obtained in JET type I ELMy H-modes with Be/W wall. Careful analysis of IR thermography data showed that both the transient ELM energy fluence and the inter-ELM power fall-off length (λ_q) are very similar in tritium and reference deuterium plasmas, within measurements uncertainties, without explicit isotope mass dependence [97]. These results give further confidence in current scaling law predictions for divertor power loads, which are only based on deuterium experiments.

6.4. Isotope mass scaling of core L-mode transport in D vs T

A dimensionless isotope mass scaling experiment was achieved in L-mode with dominant electron heating between D and T plasmas with matched dimensionless profiles $\rho_i{}^*$, ν^*, β_N, q and T_e/T_i, yielding 28% higher scaled energy confinement time in T [98]. While the isotope mass dependence is negligible for the core particle transport channel, the scaled effective heat diffusion coefficient is 50% lower in T. Local GENE simulations and flux driven ASTRA-TGLF (SAT2) simulations do not capture the measured isotope mass scaling when changing isotope mass from D to T for same input profiles. On the other hand, a similar isotope identity experiment previously carried out in H vs D had shown scaled energy confinement time and scaled core heat diffusivity independent of isotope mass and predictive JETTO-TGLF simulations in agreement with experiment [99]. Further analyses are required to clarify the origin of the different results in the H & D vs D & T L-mode isotope identity experiments, with a possible candidate being a stronger role of core ETG turbulence in the D & T identity discharges, while ITG turbulence dominated in the core plasma of the H & D identity pair.

6.5. Isotope dependence of core intrinsic rotation and Ohmic energy confinement

The isotope dependence of intrinsic toroidal rotation and ion heat transport was measured for the first time in all three hydrogen isotopes, H, D and T, in JET Ohmic plasmas by means of main ion CXRS [33] providing important information for improving predictions of intrinsic rotation and

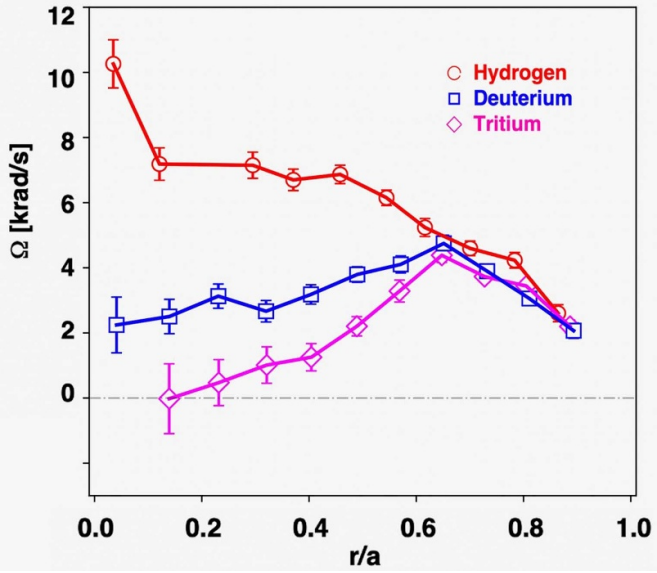

Figure 21. H, D, T toroidal angular rotation frequency profiles in JET Ohmic plasmas at 2.3 MA/2.7 T at same line averaged density $\sim 2.35 \times 10^{19}$ m^{-3} (#91634 (H) at $t = 16.41$ s, #94864 (D) at $t = 16.72$ s, #100112 (T) at $t = 16.61$ s). Reproduced from [100]. © EURATOM 2023. CC BY 4.0.

momentum transport in ITER D–T plasmas [100]. The magnitude of core plasma rotation was found to depend on isotope mass, with stronger co-current v_{tor} measured in H (see figure 21). For a given isotope, two rotation reversals were observed as a function of density [100]. The first reversal of v_{tor} occurs approximately at the change of thermal energy confinement time from the linear Ohmic confinement (LOC) to the saturated Ohmic confinement (SOC) regime [100]. The critical density for rotation reversal does not depend on isotope mass at low density but increases with isotope mass at high density. The thermal energy confinement time increases with isotope mass with scaling $\tau_{E,th} \sim A^{0.18}$ and the LOC–SOC transition shifts to a slightly higher density. Furthermore, it is demonstrated experimentally that the LOC–SOC transition occurs when the heat transport switches from electron dominated to ion dominated [101]. The isotope dependence of $\tau_{E,th}$ is only in part explained by the mass dependence of the e–i equipartition power $P_{e-i} \sim (Z^2/A)\ (n_e\ n_i/T_e^{1.5})\ (T_e - T_i)$, thus the isotope mass scaling of the ion heat diffusivity remains unexplained. Quasi-linear (TGLF-SAT2) and non-linear gyrokinetic simulations (ion-scale CGYRO) could not reproduce the experimental trends with isotope mass. Theoretical models of intrinsic rotation, based on turbulent momentum redistribution, are independent of isotope mass and therefore cannot explain the isotope dependence of the intrinsic core rotation observed in JET. However, differences in electron temperature and density profiles with different isotopes and/or an electron response to the turbulent fluctuations which depends on isotope mass, if included in future modelling with e.g. global gyrokinetic simulations, could shed light on the physics underlying the isotope dependence of intrinsic rotation [100].

7. Dependence of plasma-wall interactions on isotope mass

7.1. Be and W erosion

First observations in a tokamak environment were obtained of the impact of isotope mass on Be and W gross erosion, providing crucial input for validation of predictions of Be and W erosion and migration in ITER. In addition to the issue of erosion per se of the Be wall components in ITER, a key concern is the migration of eroded Be and formation of Be co-deposits in the inner divertor [102], which would be the dominant T-retention mechanism. Indeed, post-mortem analyses of JET-ILW tiles after three successive campaigns have shown that ∼75% of fuel retention is found in the divertor, and specifically 60% in the area on top of the inner divertor [103]. In JET, an increase in Be effective physical sputtering yield with isotope mass was measured in dedicated H, D and T Ohmic limiter plasmas, see figure 22. Spectroscopic measurements were obtained at both HFS and LFS Be limiters with visible cameras and at an inner wall Be limiter with a dedicated spectrometer LOS. The effective Be sputtering yield was obtained from the ratio of Be II 527 nm line emission to the Balmer-γ line emission and S/XB coefficients from the ADAS database [104]. The method employed to calculate the effective Be sputtering yield uses a constant value for the ratio of the S/XB coefficients, given its weak dependence on n_e and T_e for the JET Ohmic limiter plasma conditions analysed, as explained in [105]. This approximation is dictated by the lack of Langmuir probe measurements at the Be limiters and introduces an error of up to ±30% in the estimated effective Be sputtering yields, which is deemed acceptable [104]. Figure 22 shows the Be sputtering yield to first decrease with increasing density, as T_e and thereby the ion energy onto the limiter decreases, but then to increase gradually before finally dropping further with increasing density. The inflexion region of the sputtering yield vs density is an artefact of the calculation, due to the use of a constant value for the ratio of the S/XBs rather than a ratio slowly varying with n_e and T_e. However, in the comparison of Be sputtering yields of plasmas with different isotope mass shown in figure 22 the relative uncertainties are reduced to ∼±15%, as the measurements are from Ohmic limiter plasmas with very similar density and temperature. The JET measurements confirm laboratory results with H^+ and D^+ ion beams and material surface numerical simulations. The contribution of chemically assisted physical sputtering (CAPS) to the total Be gross erosion was also quantified in JET and found to be independent of hydrogen isotope mass and to vanish for Be limiter surface temperatures >400 °C–500 °C. The study of Be gross erosion yield in JET L-mode and high-power H-mode plasmas is in progress. Preliminary results indicate yields at least one order of magnitude lower than those measured in the limiter plasma experiments described above, in agreement with [102]. The Be gross erosion yields are found to decay with increasing clearance between Be limiter and last closed flux surface, as well as with increasing plasma density, these being parameters that induce a reduction in ion temperature at the limiter surfaces.

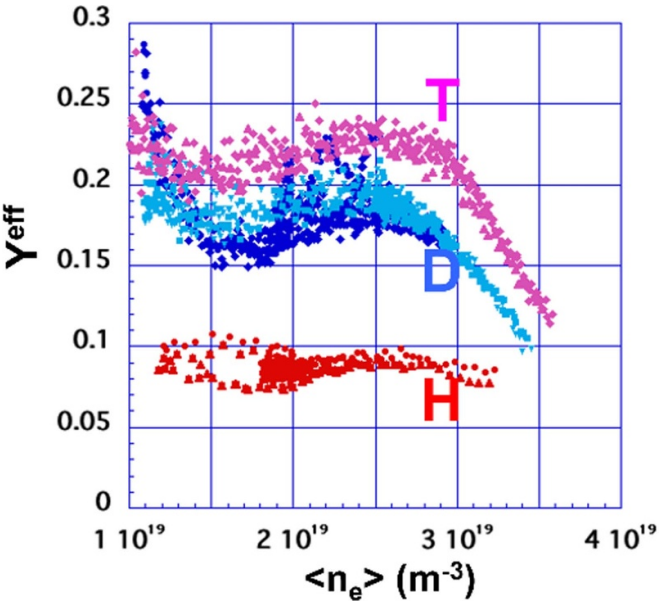

Figure 22. Effective Be sputtering yields measured at JET's inner Be limiters by visible spectroscopy. The effective Be sputtering yield was obtained from the ratio of Be II 527 nm line emission to the Balmer-γ line emission and S/XB coefficients from the ADAS database. D data are obtained from two different campaigns (marked in blue and cyan) showing excellent consistency. Data are consistent with visible camera measurements, as shown in [104]. Reproduced from [104]. © EURATOM 2022. CC BY 4.0.

In JET with Be/W wall the W gross erosion from the divertor is due to sputtering by impinging hydrogenic ions and impurity ions, primarily Be (in the absence of extrinsic impurity seeding) and is caused by a mix of intra-ELM ($E_{in} > 500$ eV) and inter-ELM ($E_{in} < 500$ eV) sputtering, where E_{in} is the impact energy of the impinging ions. Detailed measurements of effective W sputtering yields were carried out in H, D, T and D–T with optical emission spectroscopy and confirmed an increase in total W source with isotope mass [106]. Spectroscopic measurements of W CAPS were also obtained for the first time in H, D, and T from WH, WD and WT molecules, respectively (WH molecular band around 675 nm) [106]. Whereas this process provides an additional channel for W erosion, it vanishes at low T_e and its contribution to the gross W erosion is very low compared to physical sputtering.

In L-mode, the threshold energy for W physical sputtering (measured by the WI line emission at 400.9 nm relative to the Balmer-γ line emission) was found to be comparable in H, D and T plasmas. At low divertor $T_e < 40$ eV (L-mode and inter-ELM H-mode conditions) the main contribution to the effective W sputtering yield is from impurities with low Z_{eff} and is consistent with a Be ions concentration of 0.5%–1%, with effective Be sputtering increasing with isotope mass (as reported above). At high impact energies and for typical H-mode edge Be concentrations <4%, the contribution of hydrogen ions sputtering becomes important and dominates for T^+ ions over Be ions. In particular, intra-ELM W sputtering from hydrogen ions is always negligibly low for H^+ at all JET divertor temperatures, while it is dominant for D^+ and T^+ over Be ions. The total W source is found to be highest in T H-modes, indicating that inter-ELM W sputtering is also caused by T^+ ions and not only by Be sputtering (at higher impinging Be ions flux due to the stronger Be erosion in T).

Although the net W-erosion is small in JET due to high W prompt redeposition, gross W erosion by charge exchange (CX) neutral atoms in the far SOL, with poor W screening, is predicted to be substantial. Two-dimensional (2D) predictive simulations of W erosion in JET H-mode plasmas with JINTRAC (for background plasma)/ERO2.0 (for W erosion and transport) indicate perfect W screening in the divertor, but a sizeable W source into the main plasma originating from the vertical outer divertor plate (so-called Tile 8) due to sputtering by energetic impinging CX fuel atoms [107]. The CX-induced W sputtering increases with isotope mass and is thus highest in tritium and is significant for intra-ELM phases. On the other hand, there is no evidence so far from post-mortem analysis of JET tiles that the top of Tile 8 is a W erosion area. Data analysis and modelling of W sources and screening as a function of divertor strike point location, fuelling rate, ELM frequency and main fuel isotope mass are on-going to benchmark modelling workflows currently used for prediction of W erosion and transport in ITER D–T burning plasmas.

7.2. Isotope dependence of L-mode detachment and density limit

Detailed spectroscopic measurements of L-mode divertor detachment in JET-ILW in H, D, T and 40–60 D–T plasmas show stronger detachment with higher A_{eff} for the same core plasma density [108–110]. While the onset of detachment at the outer divertor occurred at the same core density for all isotope masses, the L-mode density limit was 40% lower in T. A stronger radial broadening of the SOL was measured in T than in H plasmas at the outer mid-plane, leading to increased interaction of plasma with the main chamber wall [108]. EDGE2D-EIRENE simulations are qualitatively consistent with the measurements and ascribe to the shorter ionization mean free path of T neutrals, vs D and H neutrals, the higher LFS divertor densities in T in partially detached conditions. Importantly, the detachment behaviour was measured to be independent of divertor cryo-pumping, confirming the divertor conditions to be decoupled from the particle throughput and that recycling determined the core plasma density [109]. SOL density broadening in T was also observed in H-modes, compared to D references, and is ascribed to enhanced cross field transport. Such effects were found to increase NB re-ionisation in tritium, affecting T operations [70, 111]. It remains to be assessed whether such observations could imply increased plasma-wall interaction, and thus higher wall heat loads, in D–T vs D plasmas in ITER and future power plants.

7.3. Tritium clean-up and retention

After DTE2 in 2021 and the second part of the pure T campaign which followed it in early 2022, a successful tritium cleaning experiment, using a combination of different tritium

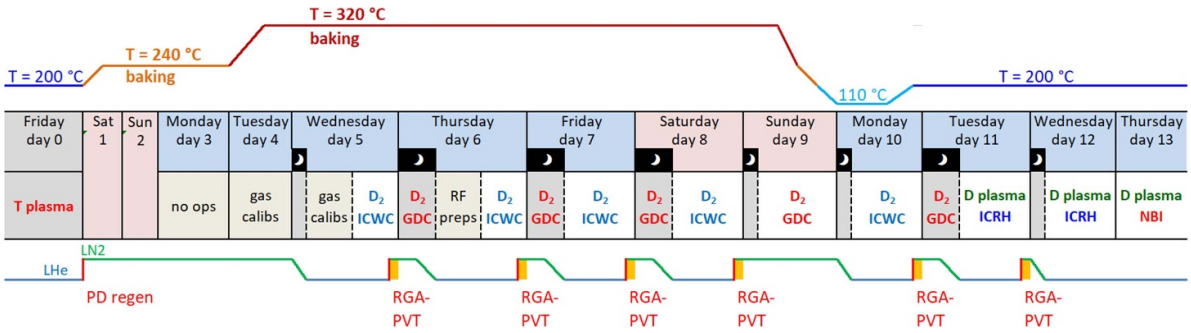

Figure 23. Experimental sequence of tritium removal after the JET-ILW T and DTE2 campaigns in 2021/22, with a combination of different tritium cleaning techniques targeting different PFC areas. The upper line shows the evolution of the vessel wall temperature with baking phase and the lower line indicates the condition of divertor cryo-pumping (PD = pumped divertor; LHe and LN2 = phases with cryo-panels at liquid He and liquid nitrogen temperatures, respectively). The moon shaped icons indicate that glow discharge cleaning (GDC) cycles and subsequent cooling down of cryo-panels to LHe were executed overnight. Reproduced from [112]. © 2023 The Author(s). Published by IOP Publishing Ltd on behalf of the IAEA. All rights reserved. CC BY 4.0.

cleaning techniques targeting a variety of PFC areas, provided key input to ITER on the efficiency of fuel removal techniques [112]. The T clean-up experiment also had the JET specific task to reduce the T content into plasma to at least 1%, to allow for subsequent plasma operation in deuterium within the allocated 14 MeV neutron budget. The total amount of T injected into the torus during the DTE2 and T campaigns in 2021/22 was 252 g, of which 17 g via NBI and 235 g via the TIMs (in DTE1 35 g of T were injected into the torus [9]). The cleaning sequence started with baking of the main chamber walls at 240 °C and 320 °C, followed by superimposed ion-cyclotron wall conditioning (ICWC) and glow discharge conditioning (GDC) in deuterium (see figure 23), preferentially accessing tritium retained in the main chamber. The final part of the cleaning sequence comprised diverted plasma operation in deuterium with different strike points configurations and ICRH or NBI heating at moderate power. In particular, the inner divertor baffle region was targeted, which is known to be the region of highest fuel retention, due to co-deposited Be layers [103]. This series of T recovery methods, previously tested successfully in 2020 for the wall change-over from D to H ahead of the tritium experiments [113], succeeded in reducing the tritium content into plasma to less than 0.1%, as quantified by D–T and D–D neutron rate measurements, much better than the goal of 1% [112]. The amount of T removed during the clean-up experiment was estimated to be 0.67 ± 0.03 g, in good agreement with T accounting by AGHS, which recorded a reduction of 0.71 g in the unaccounted amount of tritium after the clean-up experiment. In total, $\sim 4 \times 10^{23}$ T atoms were removed from JET PFCs during the clean-up sequence, ∼45% by baking and 50% by ICWC and GDC. The remaining 5% T was removed at the end of the sequence by limiter and diverted plasmas. Numerical simulations with the erosion/migration code ERO2.0 are on-going to assess the re-deposition patterns and dynamics of released material.

A further reduction of n_T/n_D to ∼0.02% was achieved during the subsequent D cleaning campaign with high power operation (see figure 24) by the time the end of T-reprocessing in the exhaust gases from torus and neutral beam injectors, and the transition to normal D operation conditions, was approved. Although the fast reduction of the T content in plasma is very promising for ITER and a reactor, per se it only indicates low T release into plasma and not necessarily low T retention in the vessel walls. The T accounting by AGHS—which quantifies the amount of T retained within the JET plant—is not completed yet and gas balance experiments in 2022 were inconclusive. Therefore, to this date, the in-vessel tritium inventory after the DTE2 and T campaigns unfortunately remains unquantified. Post-mortem analysis of JET PFCs will only be possible at the end of JET's operations in 2023. Consequently, at present one can only provide an upper bound estimate of T retention in JET with Be/W wall, based on results from gas balance analysis of D fuel retention from earlier JET-ILW campaigns, which yielded a 2% fuel retention fraction [11]. With this assumption, ∼5 g of T would have been retained in-vessel out of the 252 g injected. However, with AGHS still needing to account for ∼10 g of T to date, the current upper bound of T retention fraction is ∼4%. Until the results of the post-mortem analysis of tiles after the end of JET operations are known, the lower bound T retention can be set by the long-term D retention in JET-ILW of 0.19%, as measured by earlier post-mortem analysis [103], which would result in 0.48 g of retained tritium. These results need to be compared with the large T retention measured in JET with C-wall after DTE1: initial T inventory of 40% of the injected amount of T of 35 g, decreasing to ∼17% (∼6 g of T) after days of tokamak plasma operation in deuterium [9]. The large T retention was due primarily to co-deposited hydrocarbon layers in the divertor [9, 114]. Similar, high levels of T retention in C-wall- ∼50% short-term fuel retention-were reported after the TFTR D–T experiments in the mid 1990s [115]. These are unacceptably high levels of T retention for a fusion reactor and it was this experience that led to the decision to abandon C and choose the Be/W combination as initial wall material for ITER. JET-ILW experiments have indeed demonstrated a ten-fold reduction of fuel retention rates in D compared to reference pulses in JET-C [11]. Furthermore, first results of ASDEX-Upgrade with a full W wall and divertor had demonstrated since 2007–2008 reduced D fuel retention compared to C-dominated conditions [116].

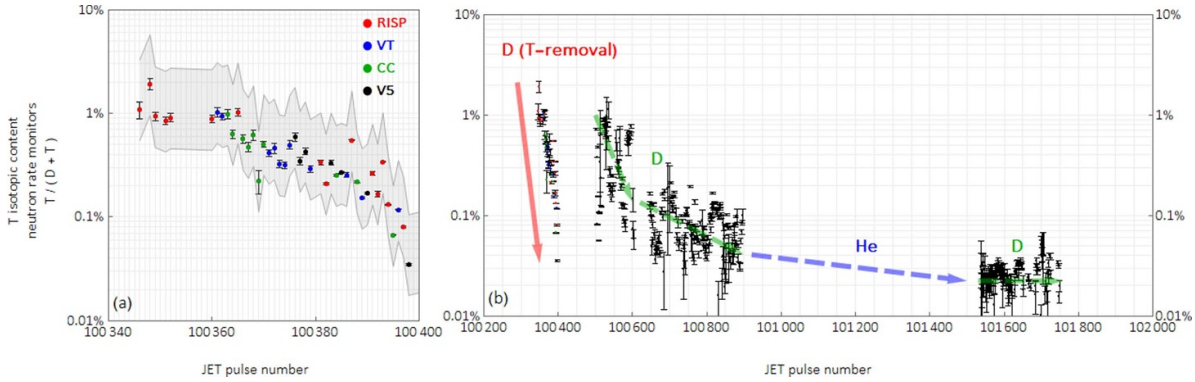

Figure 24. Decay of T content in plasma, as measured by D–D and D–T neutron rates, as a function of JET pulse number. Left figure: tritium content in divertor plasmas in the final two days of the T cleaning experiment (see sequence in figure 23), with different colour symbols denoting the different divertor configurations used in the individual pulses (see [112] for details). Right figure: decay of T content in plasma over the following months, with two D campaigns (green lines) separated by a He campaign. Data points along the red line in right figure correspond to the data from the left figure. The error bars on the individual data points indicate the statistical uncertainty dominated by 14 MeV neutron rates. The error bands in the left figure illustrate the conservative estimate of the systematic uncertainty of a factor of 2, which is due to stability issues of 14 MeV neutron monitors and the response of fission chambers changing non-linearly with incident neutron spectra [112]. Reproduced from [112]. © 2023 The Author(s). Published by IOP Publishing Ltd on behalf of the IAEA. All rights reserved. CC BY 4.0.

8. Radio-frequency heating schemes for ITER D–T operation

The high-performance hybrid and baseline scenarios in JET DTE2 used the JET workhorse H minority (/D second harmonic) ICRH heating scheme (at typically 51 MHz for $B_T \sim 3.4$ T), which has preferential electron heating. On the other hand, the versatility of the JET ICRH system was exploited in DTE2 to study the physics and relative performance of D–T ITER relevant RF schemes with preferential bulk ion heating, integrated in steady, high performance hybrid H-modes with Be/W wall [117]. This is a significant step compared to DTE1, when these RF schemes were mainly tested in ICRH-only H-modes at low density with a C-wall [118, 119].

8.1. Second harmonic heating of T and ^{3}He minority heating

Second harmonic ($N = 2$) ICRH heating of T majority ions is the reference RF heating scenario for ITER full magnetic field ($B_T = 5.3$ T) D–T plasmas and coincides with ^{3}He minority heating at fundamental resonance ($N = 1$) at a wave frequency of 53 MHz at 5.3 T [120]. In DTE2, the ($N = 2$) T RF scheme, at $f = 32.5$ MHz, was integrated and characterized in 50–50 D–T hybrid scenario H-modes at 2.3 MA/3.4 T (with 50–50 D–T plasma and 50–50 D–T NBI, as described in section 3.2). It led to high core ion heating and fusion performance, an encouraging result for ITER. Hybrid H-mode plasmas with simultaneous ^{3}He RF heating gave best results with ^{3}He concentration <2% (measured by the high-resolution Penning gauge in the sub-divertor plenum [30]), with ^{3}He introduced in the vessel by gas injection. It is to note that an intrinsic ^{3}He concentration of order 0.2%–0.4% was already measured in JET D–T plasmas before ^{3}He gas injection into the vessel, attributed to the ($^3\mathrm{H} \rightarrow {}^3\mathrm{He} + \beta^- + \nu_e$) tritium decay. RF modelling showed that even such a low intrinsic ^{3}He concentration can induce sizeable changes in ICRF power partitioning with ($N = 2$) T RF heating due to up to 30% absorption of the wave power by the ^{3}He minority [117].

While the integration of the RF schemes into steady, high performance hybrid scenario H-modes was very successful, the main challenge of these experiments was the poor reproducibility of input NBI power (22–28 MW) and RF power for direct comparison of the performance of the different RF heating schemes from pulse to pulse. In particular, P_{ICRH} decreased with decreasing RF frequency, due to a reduction in RF antenna coupling resistance, from ~4 to 4.5 MW when using 51 MHz for H minority heating/second harmonic D heating to ~3 MW when using 32.5 MHz for ^{3}He minority heating/second harmonic T heating [20]. Furthermore, the ITER-like ICRF antenna was not available for DTE2 [20]. Despite these limitations, it is possible to conclude that in 50–50 D–T hybrid H-modes, ($N = 2$) RF heating of T yielded up to 30% higher fusion power than with H minority heating at comparable total input power and gas injection rate, while the core T_i was 30% and 20% higher with ($N = 2$) T and ^{3}He minority heating, respectively, than with H minority heating [117]. NBI + ICRH modelling with PION [121] indicates that such improvement was due to a 10%–20% increase in on-axis bulk ion heating by ICRH, in addition to the NBI heating (see figure 25). The RF modelling results were also supported by experimental measurements of fast ICRF-accelerated tritons obtained with the neutral particle analyser [122] and with the magnetic proton recoil spectrometer (MPRu), especially upgraded for DTE2 [25]. For example, the time evolution of the estimated fast ion energy content due to ICRF heating, $W_{fast} \sim (P_{ICRF}\, T_e^{3/2}/n_e)$ matched the time evolution of the neutral particle fluxes of tritium at $E = 143$ keV. Synthetic neutron spectra generated by the DRESS synthetic neutron diagnostic code [123], based on the fast ion distribution function from TRANSP, were compared to the measured MPRu

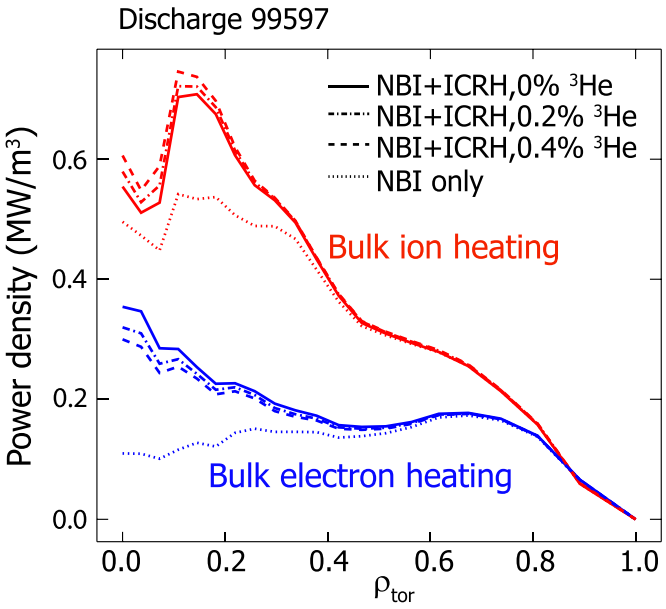

Figure 25. Collisional bulk ion heating and bulk electron heating power densities calculated by PION for JET D–T hybrid discharge #99597 ($P_{NBI} = 27.5$ MW, $P_{ICRH} = 2$ MW) with ($N = 2$) T RF heating at $t = 9.0$ s (plasma $W_{dia} = 8$ MJ), w/o ^{3}He and with ^{3}He concentration of 0.2% and 0.4%. The small-dotted lines show the simulation results for NBI-only. Reproduced from [117]. © 2023 The Author(s). Published by IOP Publishing Ltd on behalf of the IAEA. All rights reserved. CC BY 4.0.

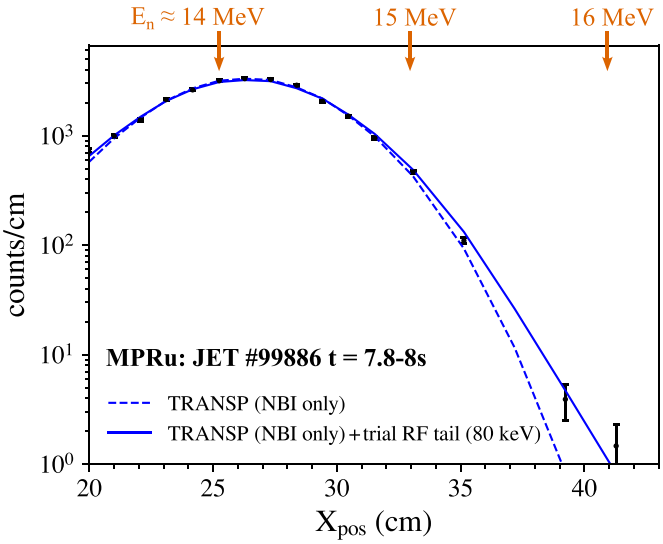

Figure 26. Neutron spectrum measured with the upgraded magnetic proton recoil spectrometer (black points) and comparison with spectra from TRANSP simulations with only NBI slowing down (dashed blue line) and with NBI + trial RF tritons tail (solid blue line), with tail temperature of 80 keV (JET D–T hybrid discharge #99886). Reproduced from [117]. © 2023 The Author(s). Published by IOP Publishing Ltd on behalf of the IAEA. All rights reserved. CC BY 4.0.

spectra to test the effect of ICRF-accelerated tritons on the total neutron spectrum [63]. Figure 26 shows one such comparison for D–T hybrid pulse # 99886, with 50–50 D–T NBI and $N = 2$ T ICRH heating. TRANSP modelling shows only a very weak modification of the fast T NBI ion distribution due to synergistic interaction with RF waves, resulting in no enhancement of the neutron rate with NBI + RF compared to the NBI only case and thus no good match with the MPRu spectrum [63]. The reason for this discrepancy deserves further investigation. For testing purposes, figure 26 shows that a fast T ion distribution function with a trial RF tail of temperature 80 keV, added to the dominant component from NBI (from TRANSP), gives best match with the measured MPRu neutron spectrum.

The results of the JET DTE2 RF studies are in contrast with those from JET DTE1 ICRH-only H-modes, which indicated poorer performance of ($N = 2$) T RF heating compared to ^{3}He minority heating. The better performance obtained in DTE2 with second harmonic T RF heating is due to the lower temperature in the tail of the distribution function of ICRF-accelerated ions (~80 keV in DTE2 experimental conditions compared to ~540 keV in DTE1), stemming from higher plasma density, lower temperature and lower ICRF power compared to the DTE1 discharges, which led to improved bulk ion heating and more peaked ICRH power deposition profiles. The DTE2 RF results are promising for ITER, where the ($N = 2$) T RF scheme would be the only auxiliary heating scheme providing dominant bulk ion heating. An additional valuable aspect of the DTE2 RF studies has been the comparison of different NBI + ICRF modelling workflows (CYRANO-FOPLA, PION-PENCIL and TORIC-TRANSP) against experiment in conditions as ITER-relevant as possible [117]. The range of modelling results obtained reflects the uncertainties stemming from the differences in the ICRF codes used and should be born in mind when assessing the DTE2 RF results or when using these codes to predict the performance of ICRF scenarios in ITER and/or other future fusion devices.

8.2. *Fundamental D minority heating*

The injection of D-NBI ions in JET at energies of ~120 keV in T-rich plasmas maximizes the beam-target fusion power (see section 2), in accordance with predictive modelling performed to guide the scenario optimization. Predictive simulations had also shown that ($N = 1$) RF heating of D minority ions can significantly boost the fusion reactivity in JET, since both the thermalized D ions and the fast D-NBI ions are accelerated to energies which are optimal for the D–T reaction cross section. While the beneficial effect of the fundamental D ICRH scheme on thermal D minority ions in tritium plasmas (without NBI) was identified in JET DTE1 experiments [3, 119], this scheme had never been tested in high performance H-mode discharges with D-NBI heating. In 2021, fundamental D ICRH heating at $f = 29$ MHz (for $B_T = 3.86$ T, see section 3.3) was tested for the first time in high power JET D–T H-mode discharges, providing efficient ion heating and strong fusion power enhancement in the T-rich hybrid plasmas with high D-NBI (see section 2), confirming the expectations from predictive modelling [38]. RF/Fokker–Planck simulations including NBI & RF synergies disentangled the different contributions

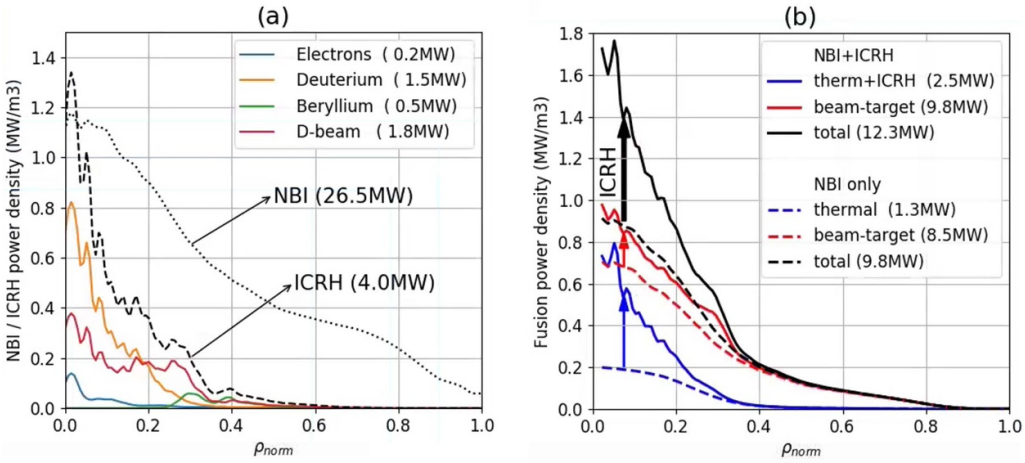

Figure 27. Results of simulations with the heating and current drive ETS workflow for JET (15–85) D–T pulse #99971 ($t = 9$ s), $B_0 = 3.85$ T, NBI heating (26.5 MW) and ICRH ($N = 1$) D minority heating, $f = 29$ MHz, (4 MW): (left) ICRF wave power absorption profiles for the different plasma species; (right) fusion power density profiles with NBI-only heating (dashed lines) and with NBI + ICRH (solid lines). Reproduced from [38]. © 2023 Crown copyright, UKAEA. CC BY 4.0.

to the record neutron yields obtained in these plasmas [38, 62]. The ICRH absorption was found to be very localized at the plasma centre inside $\rho_{\rm tor} < 0.3$ and to be dominated by the bulk D and D-NBI ions. The fusion power enhancement with RF is of order 20%, as shown in figure 27 [38, 62], and is almost equally split between the acceleration of D-beam and D-bulk ions (total $P_{\rm fus}$ increases from 9.8 MW to 12.3 MW). Looking ahead, fundamental D RF heating is expected to work well in 50–50 D–T in fusion reactors with high $T_{\rm i}$, as e.g. shown in preliminary simulations for ITER ($B_{\rm T} = 5.3$ T, $f = 40$ MHz) [124], without the need to rely on the wave absorption of D-NBI ions as in JET.

8.3. Three-ion (T-^{9}Be-D) heating scheme

A novel 3-ion (T-^{9}Be-D) RF heating scheme, profiting from the RF heating of the intrinsic ^{9}Be impurity ions at the fundamental resonance [125], was achieved for the first time in 50–50 D–T L-mode plasmas. It demonstrated efficient core plasma heating, with an increase in both core $T_{\rm i}$ and $T_{\rm e}$, increased stored energy and neutron rate, sawtooth stabilization and generation of fusion-born α-particles. This scheme was also successfully applied in a D–T H-mode in the last day of DTE2, in plasmas generating 8 MW of fusion power sustained for 2.5 s for an input power of 29 MW NBI and 1.7 MW 3-ion scheme ICRH.

9. Summary and conclusions

In this article we have presented an overview of the key physics results obtained in the recent tritium and DTE2 campaigns in JET with Be/W wall.

These experiments have demonstrated the integration of sustained, high D–T fusion performance of ELMy H-modes with the Be/W wall, a necessary and key step towards realization of $Q = 10$ in ITER. In particular, three high fusion power D–T scenarii were developed in D and realized in DTE2, investigating different fusion performance drives: (i) the 50–50 D–T baseline scenario at high plasma current (3.5 MA) and $q_{95} \sim 3$ maximized thermal fusion performance, yielding up to 8.3 MW peak fusion power in line with predictions for the given input power. Although steady and with high confinement in D, this scenario was stopped by excessive LFS edge radiation in D–T and lack of experimental time prevented its further optimization; (ii) the 50–50 D–T hybrid scenario at 2.3 MA/3.4 T ($q_{95} \sim 4.8$) achieved a best sustained fusion energy of 42 MJ, with 40% thermonuclear neutrons. A key aspect was the optimum balance between high performance and impurity control, for which maintaining a hot pedestal is a necessary requirement. Edge W impurity screening, as predicted for ITER, and enhanced by strong rotation and low collisionality was demonstrated in JET; (iii) the T-rich (15–85 D–T) hybrid scenario was designed to maximize non-thermal fusion power on JET. Consistent with modelling predictions based on the underlying physics, it achieved the highest sustained D–T fusion power, establishing the new world record of 59 MJ fusion energy.

A core-edge integrated, Ne seeded radiative H-mode was demonstrated for the first time in a 50–50 D–T mixture with the ITER-like wall. The steady, 5 s pulse, with naturally small ELMs, achieved detached divertor plasma and strongly reduced divertor temperature compared to its unseeded counterpart, confirming Ne as a promising extrinsic radiator for ITER.

A rich set of unique observations on α-particles were obtained in DTE2 in reactor relevant conditions, enabled by the new fusion diagnostics installed on JET since DTE1. Clear α-particle effects were demonstrated in DTE2, by designing experiments which minimized effects due to other fast ion populations and enabled unambiguous observation of α-particle signatures. In particular, direct evidence of electron heating by α-particles was obtained in the NBI after-glow phase of a high performance ITB scenario.

A variety of isotope experiments in T and D–T, complementing earlier datasets in H and D plasmas, advanced the understanding of the dependence of particle, heat and momentum transport on isotope mass. First ever measurements of the L–H power threshold in T and D–T with the ILW were obtained. At a given density, the L–H transition occurs for different edge power flux for different isotopes, but for the same kinetic profiles regardless of isotope mass, confirming that the L-mode edge plasma transport determines the power ($P_{\mathrm{L–H}}$) required to reach the critical profiles.

Different experiments were executed in type I ELMy H-modes to disentangle the impact of isotope mass from that of other interlinked physics parameters on heat and particle transport. A strong increase in pedestal particle confinement from D to T was observed, confirming earlier studies in H and D. At constant β_{N} and injected gas rate, the increase in pedestal pressure from D to T was primarily driven by a large increase in pedestal density due to steepening of the density gradient. Reduction in inter-ELM particle transport with increasing A_{eff}, as indicated by pedestal gyro-kinetic simulations, and improved pedestal stability, as determined by resistive MHD peeling-ballooning modes for the ELM onset, are found to be in qualitative agreement with observations. In other type I ELMy H-mode experiments, the plasma core thermal energy confinement time $\tau_{\mathrm{th,core}}$ was found to be similar for all isotope masses (H, D, T, D–T) when T_{PED} and $n_{\mathrm{e,PED}}$ could be matched by varying gas rate and plasma shaping at constant heating power. At higher pedestal stored energies, typically obtained at higher heating powers, T and D–T plasmas have higher $\tau_{\mathrm{th,core}}$ than H and D even with matched pedestal stored energies. For tritium, this $\tau_{\mathrm{th,core}}$ improvement is primarily due to the unique combination of higher $n_{\mathrm{e,PED}}$ and moderately lower $T_{\mathrm{e,PED}}$ than in H and D and higher $\nabla T/T$ to transport the same amount of heat. The measurements are broadly reproduced by quasi-linear flux driven simulations using ASTRA-TGLF (SAT2), with the pedestal experimental values (which strongly depend on A_{eff}) set as boundary condition. However, it was found that the quasi-linear modelling overestimates the core heat and particle transport both at high ($\beta_{\mathrm{N}} \sim 2.5$–3) and very low $\beta_{\mathrm{N}} \sim 1$ for all isotopes. Efforts are thus required to pinpoint the physics in TGLF at the origin of its discrepancy with experiment in these conditions.

First observations in a tokamak environment were obtained of the impact of isotope mass on Be and W gross erosion, providing crucial input for validation of predictions of Be and W erosion and migration in ITER. A successful T cleaning experiment, using a combination of different T cleaning techniques targeting different PFC areas, provided key input to ITER on the efficiency of tritium removal techniques.

The versatility of the JET ICRH system was exploited in DTE2 to study the physics and relative performance of D–T ITER relevant RF schemes with preferential bulk ion heating, integrated in steady, high performance hybrid H-modes with Be/W wall. In particular, the heating performance of the $\omega = 2\omega_{\mathrm{c}}$ (T) scheme was improved compared to the DTE1 results, which is positive news in view of ITER. Fundamental D heating was tested for the first time in high power H-modes, providing efficient ion heating and strong fusion power enhancement in the T-rich hybrid plasmas. A novel 3-ion (T-^{9}Be-D) RF heating scheme was achieved for the first time in D–T, demonstrating efficient core plasma heating and generation of α-particles. The comparison of different NBI + ICRF modelling workflows against experiment in conditions as ITER-relevant as possible provided invaluable insights on the validity of the codes used to predict the performance of ICRF scenarios in ITER and/or other future fusion devices.

By exploiting JET's unique capabilities, namely the large machine size, T handling and Be/W wall, combined with extensive heating and diagnostic enhancements since DTE1, the JET T and DTE2 experiments have provided an exceptional source of physics and engineering data to improve theory-based models, support fusion technology and accelerate ITER's research plan. Perhaps the most significant output of the experiments is the validation of current models and physics workflows in unique and ITER-relevant conditions.

The JET DTE2 experiments have demonstrated highest ever fusion energy production, in conditions closest to ITER as we can reach with any fusion facility in the world. Combining different levels of modelling complexity and promoting the combination of experiments and predictive modelling working together was key to obtaining reliable predictions of D–T plasmas starting from D plasmas. While modelling predictions of the D–T fusion power on JET-ILW have been broadly confirmed, giving confidence in fusion power predictions of ITER and future reactors, the model validation activities have also highlighted areas for improvement of self-consistent predictive modelling of D–T fusion reactors. In particular, the presence of a significant population of α-particles in burning plasmas may introduce additional physics, such as core turbulence suppression by α's, a condition which could not be tested in the JET DTE2 plasmas due to the low fraction of α-particles generated. Plasma rotation profiles were typically not predicted, but input from experiment, therefore more efforts should be invested towards maturing predictive capability of momentum transport, especially in conditions of low/no external torque input, as will be the case for ITER, DEMO and fusion power plants. The impact of MHD and Alfvén Eigenmodes on plasma energy confinement should be integrated in predictive models, as well as self-consistent predictions of impurity sources and radiation. Furthermore, the 'predict first activities' concentrated primarily on core plasma predictions, either with simple scaling from D to D–T for the pedestal or conservatively neglecting its dependence on isotope mass and SOL conditions, due to the lack of a fully predictive pedestal model encompassing self-consistently isotope mass dependence and W pedestal transport. These are key areas where intensive work should be concentrated in the near future.

Although this article refers to a set of first analyses of the JET T and DTE2 results published in 2023, it is expected that the unique wealth of data collected will generate further and more detailed analyses in the years to come.

Acknowledgments

The successful JET T and DTE2 experiments would not have been possible without the exceptional team of JET scientists, engineers and technicians who remained fully committed to achieving a common goal while facing the challenges of the COVID-19 pandemic at the same time as the technical challenges of operating JET in tritium.

This work has been carried out within the framework of the EUROfusion Consortium, funded by the European Union via the Euratom Research and Training Programme (Grant Agreement No. 101052200—EUROfusion). Views and opinions expressed are however those of the author(s) only and do not necessarily reflect those of the European Union or the European Commission. Neither the European Union nor the European Commission can be held responsible for them.

ORCID iD

C.F. Maggi https://orcid.org/0000-0001-7208-2613

References

[1] The JET Team 1992 *Nucl. Fusion* **32** 187
[2] Keilhacker M. *et al* 1999 *Nucl. Fusion* **39** 209
[3] Jacquinot J. *et al* 1999 *Nucl. Fusion* **39** 235
[4] Stork D. *et al* 2005 *Nucl. Fusion* **45** S181
[5] Strachan J.D. *et al* 1994 *Phys. Rev. Lett.* **72** 3526
[6] Hawryluk R.J. *et al* 1994 *Phys. Rev. Lett.* **72** 3530
[7] Bell M.G. *et al* 1995 *Nucl. Fusion* **35** 1429
[8] Scott S.D. *et al* 1996 *Proc. 16th Fusion Energy Conf.* (*Montreal*) vol 1 p 573
[9] Andrew P. *et al* 1999 *Fusion Eng. Des.* **47** 233
[10] Matthews G.F. *et al* 2011 *Phys. Scr.* **T145** 014001
[11] Brezinsek S. *et al* 2013 *Nucl. Fusion* **53** 083023
[12] Mailloux J. *et al* 2022 *Nucl. Fusion* **62** 042026
[13] Horton L. *et al* 2016 *Fusion Eng. Des.* **109–111** 925–36
[14] Garcia J. *et al* 2023 *Nucl. Fusion* **63** 112003
[15] Kim H.-T. *et al* 2023 *Nucl. Fusion* **63** 112004
[16] Bell A., Ballantyne P., Gordont C. and Wright M.A. 1999 *Fusion Eng. Des.* **47** 115
[17] Boyer H., Plummer D. and Johnston J. 2016 *Fusion Eng. Des.* **109–111** 1308
[18] Carvalho I. *et al* 2017 *Fusion Eng. Des.* **124** 841
[19] King D. *et al* 2023 *Nucl. Fusion* **63** 112005
[20] Jacquet P. *et al* 2023 *AIP Conf. Proc.* **2984** 030003
[21] Lässer R. *et al* 1999 *Fusion Eng. Des.* **47** 173
[22] Batistoni P. *et al* 2018 *Nucl. Fusion* **58** 026012
[23] Batistoni P. *et al* 2018 *Nucl. Fusion* **58** 106016
[24] Litaudon X. *et al* 2024 *Nucl. Fusion* **64** 112006
[25] Andersson Sunden E. *et al* 2009 *Nucl. Instrum. Meth.* A **610** 682
[26] Bonofiglo P.J., Kiptily V., Horton A., Beaumont P., Ellis R., Cecil F.E. and Podesta M. 2020 *Rev. Sci. Instrum.* **91** 093502
[27] Nocente M. *et al* 2022 *Rev. Sci. Instrum.* **93** 093520
[28] Balboa I. *et al* 2023 *Plasma Phys. Control. Fusion* **65** 064005
[29] Balboa I. *et al* 2023 *Plasma Phys. Control. Fusion* **65** 094002
[30] Vartanian S. *et al* 2021 *Fusion Eng. Des.* **170** 112511
[31] Klepper C. *et al* 2022 *IEEE Trans. Plasma Sci.* **50** 4970
[32] Klepper C. *et al* 2020 *Nucl. Fusion* **60** 016021
[33] Hawkes N., Delabie E., Menmuir S., Giroud C., Meigs A.G., Conway N.J., Biewer T.M. and Hillis D.L. 2018 *Rev. Sci. Instrum.* **89** 10D113
[34] Horton L.D. *et al* 1999 *Nucl. Fusion* **39** 993
[35] Maggi C.F. *et al* 2015 *Nucl. Fusion* **55** 113031
[36] Wesson J. 1997 *Tokamaks* (Clarendon)
[37] Štancar Ž. *et al* 2023 *Nucl. Fusion* **63** 126058
[38] Maslov M. *et al* 2023 *Nucl. Fusion* **63** 112002
[39] Field A. *et al* 2021 *Plasma Phys. Control. Fusion* **63** 095013
[40] Garzotti L. *et al* 2019 *Nucl. Fusion* **59** 076037
[41] Garcia J. *et al* 2022 *Phys. Plasmas* **29** 032505
[42] Fajardo D., Angioni C., Casson F.J., Field A.R., Maget P. and Manas P. 2023 *Plasma Phys. Control. Fusion* **65** 035021
[43] Garzotti L. *et al* 2023 Development of high current baseline scenario for high deuterium-tritium fusion performance at JET Preprint: 2023 *IAEA Fusion Energy Conf.* (London, 16–21 October 2023) EX/7-3 (available at: https://conferences.iaea.org/event/316/papers/27856/files/10983-Paper IAEA 2023 V5.pdf)
[44] Romanelli M. *et al* 2014 *Plasma Fusion Res.* **9** 3403023
[45] Bourdelle C., Citrin J., Baiocchi B., Casati A., Cottier P., Garbet X. and Imbeaux F. 2016 *Plasma Phys. Control. Fusion* **58** 014036
[46] Zotta V. *et al* 2022 *Nucl. Fusion* **62** 076024
[47] Gormezano C. *et al* 2007 Progress in the ITER physics basis *Nucl. Fusion* **47** S285
[48] Luce T.C. *et al* 2014 *Nucl. Fusion* **54** 013015
[49] Sips A.C.C. *et al* 2002 *Plasma Phys. Control. Fusion* **44** A151
[50] Wade M.R. *et al* 2003 *Nucl. Fusion* **43** 634
[51] Hobirk J. *et al* 2023 *Nucl. Fusion* **63** 112001
[52] Silburn S. *et al* 2017 *Phys. Scr.* **T170** 014040
[53] Field A. *et al* 2023 *Nucl. Fusion* **63** 016028
[54] Dux R., Loarte A., Fable E. and Kukushkin A. 2014 *Plasma Phys. Control. Fusion* **56** 124003
[55] Dux R., Loarte A., Angioni C., Coster D., Fable E. and Kallenbach A. 2017 *Nucl. Mater. Energy* **12** 28
[56] Van Vugt D.C., Huijsmans G.T.A., Hoelzl M. and Loarte A. 2019 *Phys. Plasmas* **26** 042508
[57] Casson F.J. *et al* 2020 *Nucl. Fusion* **60** 066029
[58] Ho A. *et al* 2023 *Nucl. Fusion* **63** 066014
[59] Garcia J. *et al* 2023 Overview of α-particle and fast ion studies in JET DTE2 plasmas Preprint: 2023 *IAEA Fusion Energy Conf.* (*London, 16–21 October 2023*) p EX/5–1 (available at: https://conferences.iaea.org/event/316/papers/27823/files/10746-paper v3.pdf)
[60] Maslov M. *et al* 2018 *Nucl. Fusion* **58** 076022
[61] Bourdelle C., Camenen Y., Citrin J., Marin M., Casson F.J., Koechl F. and Maslov M. 2018 *Nucl. Fusion* **58** 076028
[62] Lerche E. *et al* 2023 *AIP Conf. Proc.* **2984** 010001
[63] Kirov K.K. *et al* 2024 *Nucl. Fusion* **64** 016026
[64] Kwon J.M. *et al* 2006 *Bull. Am. Phys. Soc.* (available at: http://meetings.aps.org/link/BAPS.2006.DPP.VP1.115)
[65] Kwon J.M. *et al* 2007 *Bull. Am. Phys. Soc.* (available at: http://meetings.aps.org/link/BAPS.2007.DPP.UP8.83)
[66] Stix T.H. 1975 *Nucl. Fusion* **15** 737
[67] Kennel C.F. and Engelmann F. 1966 *Phys. Fluids* **9** 2377
[68] Giroud C. *et al* 2024 *Nucl. Fusion* **64**
[69] Marin M., Citrin J., Giroud C., Bourdelle C., Camenen Y., Garzotti L., Ho A., Sertoli M. and Contributors J. 2023 *Nucl. Fusion* **63** 016019
[70] Sun H.J. *et al* 2023 Enhanced cross-filed SOL transport in JET tritium plasma and its impact on machine operation Preprint: 2023 *IAEA Fusion Energy Conf.* (*London, 16–21 October 2023*) p 2041 (available at: https://conferences.iaea.org/event/316/papers/28175/files/10551-IAEA Sun EX-D-Divertor V3.pdf)
[71] ITER Physics Basis 1999 *Nucl. Fusion* **39** 2137

[72] Thomas P. *et al* 1998 *Phys. Rev. Lett.* **80** 5548
[73] Kiptily V. *et al* 2023 *Phys. Rev. Lett.* **131** 075101
[74] Mantica P. *et al* 2024 *Nucl. Fusion* **64** 086001
[75] Dumont R. *et al* 2018 *Nucl. Fusion* **58** 082005
[76] Fitzgerald M. *et al* 2023 *Nucl. Fusion* **63** 112006
[77] Sharapov S *et al* 2023 *Nucl. Fusion* **63** 112007
[78] Yavorskij V., Andrushchenko Z.N., Edenstrasser J.W. and Goloborod'ko V.Y. 1999 *Phys. Plasmas* **6** 3853
[79] Oliver J. *et al* 2023 *Nucl. Fusion* **63** 112008
[80] Rosenbluth M.N. and Rutherford P.H. 1975 *Phys. Rev. Lett.* **34** 1428
[81] Kiptily V.G. *et al* 2024 *Nucl. Fusion* **64** 086059
[82] Nocente M. *et al* 2021 *Rev. Sci. Instrum.* **92** 043537
[83] Solano E. *et al* 2023 *Nucl. Fusion* **63** 112011
[84] Birkenmeier G. *et al* 2023 *Plasma Phys. Control. Fusion* **65** 054001
[85] Martin Y. *et al* 2008 *J. Phys.: Conf. Ser.* **123** 012033
[86] Maggi C.F. *et al* 2018 *Plasma Phys. Control. Fusion* **60** 014045
[87] Maggi C.F. *et al* 2014 *Nucl. Fusion* **54** 023007
[88] Ryter F. *et al* 2013 *Nucl. Fusion* **53** 113003
[89] Horvath L. *et al* 2021 *Nucl. Fusion* **61** 046015
[90] Schneider P. *et al* 2022 *Nucl. Fusion* **62** 026014
[91] Frassinetti L. *et al* 2023 *Nucl. Fusion* **63** 112009
[92] Predebon I., Hatch D.R., Frassinetti L., Horvath L., Saarelma S., Chapman-Oplopoiou B., Görler T. and Maggi C.F. 2023 *Nucl. Fusion* **63** 036010
[93] Frassinetti L. *et al* 2017 *Nucl. Fusion* **57** 016012
[94] Frassinetti L. *et al* 2017 *Plasma Phys. Control. Fusion* **59** 014014
[95] Nyoström H., Frassinetti L., Saarelma S., Huijsmans G.T.A., Perez von Thun C., Maggi C.F. and Hillesheim J.C. (JET Contributors) 2023 *Nucl. Fusion* **62** 126045
[96] Schneider P. *et al* 2023 *Nucl. Fusion* **63** 112010
[97] Faitsch M., Balboa I., Lomas P., Silburn S.A., Tookey A., Kos D., Huber A., de la Luna E., Keeling D. and Kappatou A. 2023 *Nucl. Fusion* **63** 112013
[98] Tala T. *et al* 2023 *Nucl. Fusion* **63** 112012
[99] Maggi C.F. *et al* 2019 *Nucl. Fusion* **59** 076028
[100] Nave F. *et al* 2023 *Nucl. Fusion* **63** 044002
[101] Delabie E. *et al* 2023 The isotope effect on core heat transport in JET-ILW ohmic plasmas in hydrogen, deuterium and tritium Preprint: 2023 *IAEA Fusion Energy Conf.* (*London*, *16–21 October 2023*) p 1982 (available at: https://conferences.iaea.org/event/316/contributions/28087/attachments/14509/23795/Delabie-EX-C.pdf)
[102] Romazanov J. *et al* 2019 *Nucl. Mater. Energy* **18** 331
[103] Widdowson A. *et al* 2021 *Phys. Scr.* **96** 124075
[104] De La Cal E. *et al* 2022 *Nucl. Fusion* **62** 126021
[105] De La Cal E. *et al* 2022 *Nucl. Fusion* **62** 126001
[106] Douai D. *et al* 2023 Overview of plasma-wall interactions studies in JET-ILW H, D, T and DT campaigns Preprint: 2023 *IAEA Fusion Energy Conf.* (*London*, *16–21 October 2023*) p EX/8–5 (available at: https://conferences.iaea.org/event/316/papers/27863/files/11163-MANUSCRIPT%DOUAI-EX-D.pdf)
[107] Kumpulainen H.A. *et al* 2022 *Nucl. Mater. Energy* **33** 101264
[108] Groth M. *et al* 2023 Impact of H, D, T and D-T hydrogenic isotopes on detachment in JET ITER-like wall low-confinement mode plasmas Preprint: 2023 *IAEA Fusion Energy Conf.* (*London*, *16–21 October 2023*) p EX/8–2 (available at: https://conferences.iaea.org/event/316/papers/27861/files/10630-MGroth PWJET1CP23 33904 submitted.pdf)
[109] Groth M. *et al* 2023 *Nucl. Mater. Energy* **34** 101345
[110] Solokha V. *et al* 2020 *Phys. Scr.* **T171** 014039
[111] King D. *et al* 2024 *Nucl. Fusion* **64** 106014
[112] Matveev D. *et al* 2023 *Nucl. Fusion* **63** 112014
[113] Wauters T. *et al* 2022 *Phys. Scr.* **97** 044001
[114] Loarer T. *et al* 2013 *J. Nucl. Mater.* **438** S108
[115] Mueller D. *et al* 1997 *J. Nucl. Mater.* **241–243** 897
[116] Zohm H. *et al* 2009 *Nucl. Fusion* **49** 104009
[117] Mantsinen M. *et al* 2023 *Nucl. Fusion* **63** 112015
[118] Start D. *et al* 1998 *Phys. Rev. Lett.* **80** 4681
[119] Start D. *et al* 1999 *Nucl. Fusion* **39** 321
[120] ITER Organization 2018 ITER research plan within the staged approach (level III—provisional version) ITER Technical Report No. ITR-18-003 (available at: www.iter.org/doc/www/content/com/Lists/ITER%20Technical%20Reports/Attachments/9/ITER-Research-Plan_final_ITR_FINAL-Cover_High-Res.pdf)
[121] Eriksson L.G., Hellsten T. and Willen U. 1993 *Nucl. Fusion* **33** 1037
[122] Siren P., Beaumont P. and Weisen H. 2022 *JINST* **17** C08006
[123] Baeumel S. *et al* 2004 *Rev. Sci. Instrum.* **75** 3563
[124] Schneider M., Lerche E., Van Eester D., Hoenen O., Jonsson T., Mitterauer V., Pinches S.D., Polevoi A.R., Poli E. and Reich M. 2021 *Nucl. Fusion* **61** 126058
[125] Kazakov Y., Ongena J., Van Eester D., Bilato R., Dumont R., Lerche E., Mantsinen M. and Messiaen A. 2015 *Phys. Plasmas* **22** 082511